

Spin-orbit coupling in wurtzite quantum wells

J. Y. Fu,^{1,2,*} P. H. Penteado,^{2,*} D. R. Candido,^{2,3,4} G. J. Ferreira,⁵ D. P. Pires,^{2,6} E. Bernardes,² and J. C. Egues²

¹Department of Physics, Qufu Normal University, Qufu, Shandong, 273165, China

²Instituto de Física de São Carlos, Universidade de São Paulo, 13560-970 São Carlos, São Paulo, Brazil

³Department of Physics and Astronomy, University of Iowa, Iowa City, Iowa 52242, USA

⁴Pritzker School of Molecular Engineering, University of Chicago, Chicago, Illinois 60637, USA

⁵Instituto de Física, Universidade Federal de Uberlândia, Uberlândia, Minas Gerais 38400-902, Brazil

⁶Departamento de Física Teórica e Experimental, Universidade Federal do Rio Grande do Norte, 59072-970 Natal, Rio Grande do Norte, Brazil

(Dated: October 10, 2021)

Effective spin-orbit (SO) Hamiltonians for conduction electrons in wurtzite heterostructures are lacking in the literature, in contrast to zincblende structures. Here we address this issue by deriving such an effective Hamiltonian valid for quantum wells, wires, and dots with arbitrary confining potentials and external magnetic fields. We start from an 8×8 Kane model accounting for the s - p_z orbital mixing important to wurtzite structures, but absent in zincblende, and apply both quasi-degenerate perturbation theory (Löwdin partitioning) and the folding down approach to derive an effective 2×2 electron Hamiltonian. Focusing on wurtzite quantum wells, we later on also perform a self-consistent Poisson-Schrödinger calculation in the Hartree approximation to determine the relevant SO couplings. We obtain the usual k -linear Rashba term arising from the structural inversion asymmetry of the wells and, differently from zincblende structures, a bulk Rashba-type term induced by the inversion asymmetry of the wurtzite lattice. Our results show this latter term to be the main contribution to the Rashba coupling in wurtzite wells. We also find linear- and cubic-in-momentum Dresselhaus contributions. Both the bulk Rashba-type term and the Dresselhaus terms originate exclusively from the admixture of s - and p_z -like states in wurtzites structures. Interestingly, in these systems the linear Rashba and the Dresselhaus terms have the same symmetry and can in principle cancel each other out completely, thus making the spin a conserved quantity. We determine the intrasubband (intersubband) Rashba α_ν (η) and linear Dresselhaus β_ν (Γ) SO strengths of GaN/AlGa_{0.3}N single and double wells with one and two occupied subbands ($\nu = 1, 2$). For the GaN/Al_{0.3}Ga_{0.7}N single well with one occupied subband, we obtain the total spin splitting coefficient $\alpha_1^{\text{eff}} = \alpha_1 + \beta_1 \sim 7.16$ meV-Å, in agreement with weak antilocalization measurements. In the case of two occupied subbands, we observe that the intersubband Rashba η is much weaker than the intrasubband coupling α_ν . For double wells even in the presence of strong built-in electric fields (spontaneous and piezoelectric, crucial in GaN/AlGa_{0.3}N wells), we find a *seemingly* symmetric potential configuration at which both the Rashba η and Dresselhaus Γ intersubband couplings exhibit their highest strengths. On the other hand, we observe that the intrasubband Dresselhaus coefficients β_1 and β_2 interchange their values as the gate voltage V_g varies across zero; a similar behavior, though less pronounced, is seen for the Rashba couplings α_1 and α_2 . We believe our general effective Hamiltonian for electrons in wurtzite heterostructures put forward here, should stimulate additional theoretical works on wurtzite quantum wells, wires, and dots with variously defined geometries and external magnetic fields.

PACS numbers: 71.70.Ej, 85.75.-d, 81.07.St

I. INTRODUCTION

The spin-orbit interaction couples the electron spin and its momentum. While in atomic systems this relativistic effect arises from the Coulomb interaction within the atom, in mesoscopic semiconductor heterostructures such as quantum wells, wires, and dots, the SO interaction originates from the interplay of the confining, doping, Hartree, and external gate potentials. Unlike atomic systems, the SO coupling strength in these systems can be electrically controlled, thus providing a unique handle for the manipulation of the magnetic moment of the electron. Spin manipulation via the SO interaction is an important resource in spintronic devices and quantum information processing with spin qubits [1, 2].

Spin orbit effects also underlie novel topological transport

phenomena in diverse fields of quantum condensed matter such as topological insulators [3, 4], Majorana fermions [5–7], and Weyl semimetals [8]. Recent proposals for stretchable [9] spin helix [10–13] and persistent skyrmion lattice excitations [14] in ordinary GaAs wells also highlight the important role of the SO in quantum wells.

So far, detailed theoretical and experimental studies on the SO coupling in semiconductors have been performed mostly in crystals with zincblende structure, including both bulk and confined systems [15, 16]. It is well established by now that the structural inversion asymmetry (SIA) of wells lead to a linear-in-momentum Rashba term [17] while the bulk inversion asymmetry (BIA) of the underlying zincblende crystal lattice gives rise to linear- and cubic-in-momentum Dresselhaus terms [18]. Wells with two subbands also have *intersubband* Rashba- and Dresselhaus-like terms [14, 15, 19, 20]. The interplay of the linear Rashba and Dresselhaus terms gives rise to some of the interesting phenomena mentioned in the previous paragraph in zincblende matrices.

* These authors contributed equally to this work.

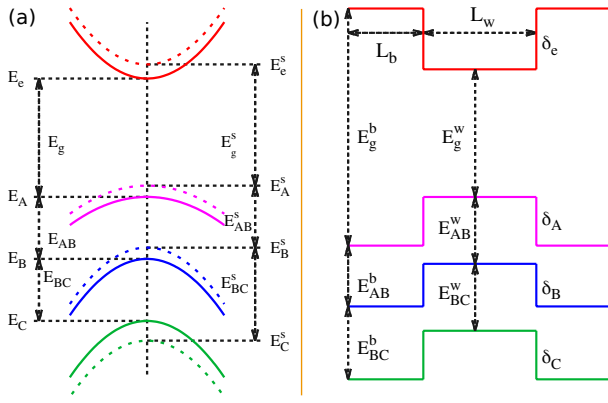


Figure 1. (a) Schematic of the dispersion relation (Chuang and Chang basis set) of an unstrained (solid curves) and a strained (dashed curves) wurtzite semiconductor close to the Γ point ($k = 0$). The superscript s in the band parameters indicates the strained case. (b) Potential profile of a wurtzite single well of width L_w and barriers of width L_b . The superscripts b and w stand for barrier and well, respectively. No s - p_z mixing is considered here since its effect is negligible on the band edges at the Γ point.

On the other hand, in wurtzite structures, the presence of a hexagonal c axis along the z || (0001) direction allows for a linear BIA Rashba term [21, 22] in addition to a cubic BIA Dresselhaus term [23, 24]. Besides these BIA terms, a usual SIA Rashba-like contribution [17] is also present in wurtzite wells as we shall see.

The SO coupling in wurtzite semiconductors has attracted interest both experimentally [25–34] and theoretically [23, 24, 35, 36]. Experimentally, spin splitting energies from 0 up to 13 meV were reported in GaN-based heterostructures [25, 29–31, 33]. Weak antilocalization measurements provide a SO splitting parameter value ranging from 5.5 to 10.01 meV·Å [26–28, 30, 32, 34]. Compared with these measurements, the value extracted from the beating pattern of Shubnikov-de Haas oscillations is very large, around 65 meV·Å, which is attributed to the structural inhomogeneity of the crystals [37, 38].

Theoretically, Lew Yan Voon *et al.* investigated the linear Rashba-type term in bulk wurtzite semiconductors [35] and found that the linear term is mainly determined by the mixing of the s orbital of the conduction band and the p_z orbital of the valence band (s - p_z mixing) [39]. Wang *et al.* studied the bulk cubic Dresselhaus SO interaction and demonstrated the existence of a zero Dresselhaus spin splitting surface in wurtzite semiconductors [23]. Fu and Wu evaluated the bulk Dresselhaus coefficient in GaN, 0.32 eV·Å³ [24], which has been experimentally verified via the circular photogalvanic measurement [40]. More recently, Faria Junior *et al.* [41] investigated the bulk spin-orbit coupling effect in the wurtzite phase via *ab initio* band structure calculations.

In addition to studies on the bulk wurtzite structure, the SO coupling parameter in GaN/AlN heterostructures, around 8 meV·Å, was determined by Majewski via first-principles calculations [42]. Litvinov investigated the spin splitting of GaN/AlGaAs heterostructure [36] and GaN/InGaN quantum

wells [43], with one occupied electronic subband. Following the basic framework of his formulation, Li *et al.* determined the Rashba couplings associated with two occupied electronic subbands in GaN/Al_{0.3}Ga_{0.7}N wells, $\alpha_1 \approx \alpha_2 \sim 0.5$ meV·Å.

Although several investigations have been conducted, a comprehensive theory on the SO coupling in wurtzite crystals, from bulk to confined structures, is still lacking in the literature. Moreover, for the available reports on the SO coupling, the s - p_z orbital mixing, which we find is crucial in obtaining certain SO terms, was not taken into account in the Kane models used. In addition, in the derivation of the effective electron Hamiltonian, the renormalization of the conduction band spinor component was not considered [36], thus leading to an energy dependent Schrödinger-type equation.

In this work, we account for these missing ingredients and establish a detailed systematic formulation for the electron SO interaction in wurtzite heterostructures. We then consider GaN/AlGaN wells, both single and double, involving the electron occupancy of either one or two subbands, and self-consistently determine the intrasubband (intersubband) Rashba α_ν (η), $\nu = 1, 2$, and Dresselhaus β_ν (Γ) terms. By using an external gate voltage V_g , we also discuss the electrical control of all relevant SO couplings. These SO terms are helpful to investigate spin related properties in semiconductors with wurtzite phase, especially in confined wurtzite nanostructures (wells, wires, and dots).

More specifically, we use the basis set defined by Chuang and Chang [44] (“CC basis”) to construct an 8×8 Kane model, in which we account for the s - p_z orbital mixing (see Appendix A). The CC basis (Table I) is a solution of the bulk Hamiltonian at $k = 0$ (Γ point) with the k -independent SO coupling being partially included [Eq. (4)]. Therefore, the Kane model contains nonzero off-diagonal elements even at $k = 0$ [see Eq. (7)], implying that the diagonal elements of the Kane matrix in general do not describe the actual band edge energies, Fig. 1. We also derive the bulk Kane Hamiltonian in the “diagonal basis”, in which the Kane model is diagonal at $k = 0$ (Appendix B). This helps us determine the diagonal elements (not actual band edge energies) of the Kane model in the CC basis as well as the corresponding “virtual” band offsets (see Table II). Having the bulk Kane model at hand, we then construct its analogue for heterostructures.

We use quasi-degenerate perturbation theory (Löwdin partitioning) [45] and the folding down approach [19, 20] to derive an effective 2×2 electron Hamiltonian [Eq.(24)] from the 8×8 Kane model for wurtzite heterostructures. As opposed to what has been reported in the literature [36, 46, 47], we arrive at a *genuine* Schrödinger-type equation, i.e., an energy-independent effective Hamiltonian, since we account for the renormalization of the conduction band spinor component (Appendix C).

In addition to the usual linear in momentum Rashba term induced by the structural inversion asymmetry of the wells, see Eqs. (33) and (34), we obtain a bulk Rashba-type SO coupling as a function of the s - p_z orbital mixing [Eq. (32)]. Within the eight bands considered (s -conduction and p -valence bands), the $k \cdot p$ interaction accounted for in the valence band subspace gives rise to the Dresselhaus cou-

pling (Appendix D). This is in contrast to systems with the zincblende structure, in which the Dresselhaus term is only present if the $\mathbf{k} \cdot \mathbf{p}$ interaction with remote bands, e.g., the p -conduction band, is included [48]. We also derive a general effective electron Hamiltonian containing all relevant SO terms for wurtzite nanostructures in the presence of a magnetic field and an arbitrary 3D confinement [see Eqs. (36)–(39)].

Based on our results for the SO terms, we self-consistently calculate the total spin splitting coefficient for a GaN/AlGaIn single well with one occupied subband $\alpha_1^{\text{eff}} = \alpha_1 + \beta_1 \sim 7.16$ meV·Å [Figs. 2–4], in agreement with weak antilocalization measurements [28, 30, 34]. We determine as well the several distinct terms composing the Rashba SO coupling: the “bulk” [49], the Hartree, and the structural well contributions [Eq. (31)], and show that the strength of the SO coupling follows from the interplay of all these components, Fig. 3. For a similar calculation for zincblende quantum wells see Refs. [19, 20]. We note that the bulk Rashba term dominates over all the other contributions. Accordingly, the latter remains essentially constant as a function of the gate voltage V_g , Fig. 3(a). When the wells have two occupied subbands (higher electron density), we find that the intersubband Rashba strength η is much weaker than the intrasubband coupling α_ν , Fig 5.

On the other hand, for GaN/AlGaIn double wells [Fig. 6], interestingly, we find a *seemingly* symmetric configuration depending on the relative ratio of the Al content between the central and lateral barriers, even in the presence of the strong built-in electric field (spontaneous and piezoelectric). At this configuration, a maximal strength of the intersubband Rashba η and Dresselhaus Γ couplings occurs. In addition, by varying V_g we observe that the Dresselhaus couplings β_1 and β_2 change dramatically and almost interchange their values. Although less pronounced, a similar behavior also holds for the Rashba couplings α_1 and α_2 , see Fig. 7.

The paper is organized as follows. In Secs. II–IV, we present the model and method used. Specifically, in Sec. II, we review the $\mathbf{k} \cdot \mathbf{p}$ method and apply it to obtain an 8×8 Kane model for both unstrained and strained wurtzite wells. In Sec. III, we derive a 2×2 3D SO Hamiltonian for electrons from the Kane model obtained in Sec. II. In this derivation, we use both the Löwdin partitioning method and the folding down approach. By projecting the 3D Hamiltonian onto the quantum well subbands (obtained in a self-consistent way), we derive in Sec. IV an effective 2D electron Hamiltonian containing all the relevant SO terms. For concreteness, we present and discuss numerical results for GaN/AlGaIn wells in Sec. V. We summarize our main findings in Sec. VI.

II. 8×8 KANE MODEL: BULK \rightarrow HETEROSTRUCTURES

A. The $\mathbf{k} \cdot \mathbf{p}$ method: general remarks and notation

For an electron on a microscopic periodic potential $V(\mathbf{r})$, the Schrödinger equation for the periodic part $u_{\nu\mathbf{k}}(\mathbf{r})$ of the

Bloch function is given by [16, 50, 51]

$$\left[\frac{p^2}{2m_0} + V(\mathbf{r}) + H_{\text{so}} + \frac{\hbar}{m_0} \mathbf{k} \cdot \boldsymbol{\pi} \right] u_{\nu\mathbf{k}}(\mathbf{r}) = \left(E_\nu(\mathbf{k}) - \frac{\hbar^2 k^2}{2m_0} \right) u_{\nu\mathbf{k}}(\mathbf{r}), \quad (1)$$

where m_0 is the bare electron mass, ν is a band index for each wave vector \mathbf{k} , \mathbf{p} is the momentum operator, and

$$\boldsymbol{\pi} = \mathbf{p} + \frac{\hbar}{4m_0 c^2} \boldsymbol{\sigma} \times \nabla V(\mathbf{r}), \quad (2)$$

with $\boldsymbol{\sigma} = (\sigma_x, \sigma_y, \sigma_z)$ being the Pauli matrices. The spin-orbit coupling appears in Eq. (1) as the $\mathbf{k} = 0$ term

$$H_{\text{so}} = \frac{\hbar}{4m_0^2 c^2} \nabla V(\mathbf{r}) \times \mathbf{p} \cdot \boldsymbol{\sigma}, \quad (3)$$

and the \mathbf{k} -linear term $\frac{\hbar}{m_0} \mathbf{k} \cdot \boldsymbol{\pi}$.

The Hamiltonian above considers an unstrained crystal. For a finite strain, one must add the strain related couplings H_{strain} to Eq. (1) [52, 53]. We will discuss the strain tensor and its effects in Section II B 3.

To solve Eq. (1) in the vicinity of the Γ point ($\mathbf{k} \approx 0$) within the $\mathbf{k} \cdot \mathbf{p}$ approach, one must define a basis set $\{u_{\nu 0}(\mathbf{r})\}$ at $\mathbf{k} = 0$ to expand $u_{\nu\mathbf{k}}(\mathbf{r})$. This choice of basis set is in principle not unique and leads to different representations of the Kane model [16, 51]. Ideally, one would prefer to work on a basis set that diagonalizes Eq. (1) at $\mathbf{k} = 0$, as it is commonly done for zincblende structures. However, it is often more interesting to use a basis defined by the irreducible representations (IRREPs) of the crystal’s group, which is not always diagonal at $\mathbf{k} = 0$. This is the case for the basis set defined by Chuang and Chang [44] and introduced in the next section.

B. 8×8 Kane model: bulk

In the following sections, we build an 8×8 bulk Kane model (unstrained/strained) for wurtzite crystals using a slightly modified CC basis (primed basis CC' , see Appendix A), which incorporates previously neglected effects of the s - p_z coupling [35].

1. CC basis: unstrained case

Our basis set is defined by splitting the total Hamiltonian in Eq. (1) as $H = H_0^{\text{CC}} + W^{\text{CC}}(\mathbf{k})$, with

$$H_0^{\text{CC}} = \frac{p^2}{2m_0} + V(\mathbf{r}) + H_{\text{so}z}, \quad (4)$$

$$W^{\text{CC}}(\mathbf{k}) = \frac{\hbar}{m_0} \mathbf{k} \cdot \boldsymbol{\pi} + H_{\text{so}x} + H_{\text{so}y}, \quad (5)$$

$$H_{\text{so}j} = \frac{\hbar}{4m_0^2 c^2} \left(\nabla V(\mathbf{r}) \times \mathbf{p} \right)_j \sigma_j, \quad (6)$$

where $j = \{x, y, z\}$ labels the spin components of H_{so} . The chosen CC basis is composed by the eigenstates that diagonalize H_0^{CC} , which includes only the z -component ($H_{\text{so}z}$) of the $\mathbf{k} = 0$ spin-orbit interaction. Therefore, our Hamiltonian will not be diagonal at $\mathbf{k} = 0$, since the perturbation $W^{\text{CC}}(\mathbf{k})$ contains the \mathbf{k} -independent $H_{\text{so}x}$ and $H_{\text{so}y}$ terms.

Wurtzite crystals comprise two interpenetrating hexagonal lattices that transform according to the space group $P6_3mc$ (C_{6v}^4), yielding the C_{6v} point group at Γ ($\mathbf{k} = 0$). Hence, the solutions of H_0^{CC} are given by single-group states belonging to

$$H_{8 \times 8}^{\text{CC}} = \frac{p^2}{2m_0} + \begin{pmatrix} 0 & 0 & -\frac{1}{\sqrt{2}}P_2k_+ & 0 & \frac{1}{\sqrt{2}}P_2k_- & -i\sqrt{2}\Delta_{sz} & P_1k_z & 0 \\ 0 & 0 & 0 & \frac{1}{\sqrt{2}}P_2k_- & -i\sqrt{2}\Delta_{sz} & -\frac{1}{\sqrt{2}}P_2k_+ & 0 & P_1k_z \\ -\frac{1}{\sqrt{2}}P_2k_- & 0 & -E_g^{\text{CC}} & 0 & 0 & 0 & 0 & 0 \\ 0 & \frac{1}{\sqrt{2}}P_2k_+ & 0 & -E_g^{\text{CC}} & 0 & 0 & 0 & 0 \\ \frac{1}{\sqrt{2}}P_2k_+ & i\sqrt{2}\Delta_{sz} & 0 & 0 & -E_g^{\text{CC}} - E_{AB} & 0 & 0 & \sqrt{2}\Delta_3 \\ i\sqrt{2}\Delta_{sz} & -\frac{1}{\sqrt{2}}P_2k_- & 0 & 0 & 0 & -E_g^{\text{CC}} - E_{AB} & \sqrt{2}\Delta_3 & 0 \\ P_1k_z & 0 & 0 & 0 & 0 & \sqrt{2}\Delta_3 & -E_g^{\text{CC}} - E_{AC} & 0 \\ 0 & P_1k_z & 0 & 0 & \sqrt{2}\Delta_3 & 0 & 0 & -E_g^{\text{CC}} - E_{AC} \end{pmatrix}. \quad (7)$$

Table I. CC basis functions $u_{\nu 0}^{\text{CC}}(\mathbf{r}) \equiv u_{\nu 0}(\mathbf{r}) \equiv \langle \mathbf{r} | \nu \rangle$, with $\nu=1, 2, \dots, 8$. The states $|S'\rangle$ and $|Z'\rangle$ transform like scalars and $\{|X\rangle, |Y\rangle\}$ transform like vectors. The corresponding doubly-degenerate band edges (at the Γ point) are denoted by E_e (conduction) and E_A, E_B, E_C (valence) bands, respectively. The s - p_z mixed orbitals are $|S'\rangle = q_s |S\rangle + q_z |Z\rangle$, and $|Z'\rangle = q_s |Z\rangle - q_z |S\rangle$, with $q_s^2 + q_z^2 = 1$ and $q_z \ll 1$ (Appendix A).

	ν	$ \nu\rangle$	C_{6v} IRREP
e	1	$ iS'\uparrow\rangle$	Γ_1
e	2	$ iS'\downarrow\rangle$	Γ_1
A	3	$-\frac{1}{\sqrt{2}} X+iY\rangle$	Γ_5
A	4	$+\frac{1}{\sqrt{2}} X-iY\rangle$	Γ_5
B	5	$+\frac{1}{\sqrt{2}} X-iY\rangle$	Γ_5
B	6	$-\frac{1}{\sqrt{2}} X+iY\rangle$	Γ_5
C	7	$ Z'\uparrow\rangle$	Γ_1
C	8	$ Z'\downarrow\rangle$	Γ_1

The nonzero matrix element Δ_{sz} was neglected in the original work by Chuang and Chang [44], see Appendix A for details on the origin of this term. However, it is allowed by symmetry as mentioned above. Namely, this spin-orbit coupling reads

$$\Delta_{sz} = \frac{\hbar^2}{4m_0^2c^2} \langle Y | \frac{\partial V}{\partial y} \frac{\partial}{\partial z} - \frac{\partial V}{\partial z} \frac{\partial}{\partial y} | S' \rangle. \quad (8)$$

Even though this term has a negligible effect on the band edges at $\mathbf{k} = 0$, it is crucial in obtaining the relevant SO terms

the Γ_1 (S and Z) and Γ_5 ($\{X, Y\}$) IRREPs of C_{6v} , with well defined spin (\uparrow and \downarrow) along the z direction. Note that differently from zincblende crystals, the z direction in the wurtzite unit cell is nonequivalent to the x and y directions. This allows for an s - p_z mixing [35, 39], thus leading to the hybridized S' and Z' orbitals shown in Table I.

Using the CC basis listed in Table I [$|\nu\rangle$ states in Table III, Appendix A], we can now build the bulk 8×8 Kane Hamiltonian $H_{8 \times 8}^{\text{CC}}$. We find [54] (see Appendix A 4)

at $\mathbf{k} \neq 0$.

The diagonal matrix elements in (7) are the eigenenergies of H_0^{CC} [see Eq. (4)]; here we set $E_e \equiv 0$ (energy reference), $E_A = -E_g^{\text{CC}}$, $E_B = -E_g^{\text{CC}} - E_{AB}$, and $E_C = -E_g^{\text{CC}} - E_{AC}$, with the subscripts e denoting the lowest conduction band and A, B , and C the topmost three valence bands, respectively. The term $E_g^{\text{CC}} \approx E_g$ corresponds to the band gap (see discussion below). The energy differences between the valence band edges are given by

$$E_{AB} = 2\Delta_2, \quad E_{AC} = \Delta_1 + \Delta_2, \quad (9)$$

where $\Delta_1 \equiv \Delta_{\text{cr}}$ is the crystal-field splitting energy, and Δ_2 and Δ_3 are two SO split-off energy parameters, which read

$$\Delta_2 = -\frac{\hbar^2}{4m_0^2c^2} \langle Y | \frac{\partial V}{\partial x} \frac{\partial}{\partial y} - \frac{\partial V}{\partial y} \frac{\partial}{\partial x} | X \rangle, \quad (10)$$

$$\Delta_3 = \frac{\hbar^2}{4m_0^2c^2} \langle Y | \frac{\partial V}{\partial y} \frac{\partial}{\partial z} - \frac{\partial V}{\partial z} \frac{\partial}{\partial y} | Z \rangle.$$

These are commonly assumed to be related by $\Delta_2 = \Delta_3 \equiv \Delta_{\text{so}}/3$ [55], following the quasi-cubic approximation [51]. The off-diagonal \mathbf{k} -linear terms are defined by Kane parameters $P_1 = -(i\hbar/m_0) \langle S' | p_z | Z \rangle$ and $P_2 = -(i\hbar/m_0) \langle S' | p_x | X \rangle = -(i\hbar/m_0) \langle S | p_y | Y \rangle$, with $k_{\pm} = k_x \pm ik_y$.

The Hamiltonian in Eq. (7) is well defined in terms of the matrix elements shown above. Note, however, that the diagonal matrix elements do not correspond to the real band

edges, since $H_{8 \times 8}^{\text{CC}}$ is not diagonal at $k = 0$. Nevertheless, we can safely use $E_g^{\text{CC}} \approx E_g$ (real band gap) since (i) Eq. (7) shows that the topmost valence band A does not couple to other bands at $k = 0$, and (ii) the Δ_{sz} coupling between the conduction and valence bands leads to a negligible second-order correction for the conduction band at $k = 0$, i.e., $E_g = E_g^{\text{CC}} - 2\Delta_{sz}^2/(E_g^{\text{CC}} + E_{AB}) \approx E_g^{\text{CC}}$.

In the following, we derive the bulk Rashba term (see Appendix A 4 for more details).

2. Bulk Rashba dispersion

The conduction band of wurtzite crystals has intrinsic Rashba-like spin textures [21]; this interesting feature was associated with the s - p_z mixing [35]. To obtain a closed expression for this spin-orbit coupling within our model, we use Löwdin perturbation theory to derive an effective 2×2 bulk Hamiltonian for the conduction band. Up to fourth order, we obtain

$$H_{2 \times 2}^{\text{CC}} = \frac{\hbar^2 k_z^2}{2m_{\perp}} + \frac{\hbar^2 k_{\parallel}^2}{2m_{\parallel}} + \alpha_{\text{bulk}} (\sigma_x k_y - \sigma_y k_x), \quad (11)$$

with $k_{\parallel}^2 = k_x^2 + k_y^2$, effective masses

$$\frac{1}{m_{\perp}} = \frac{1}{m_0} + \frac{2P_1^2}{\hbar^2} \frac{1}{E_g + \Delta_1 + \Delta_2}, \quad (12)$$

$$\frac{1}{m_{\parallel}} = \frac{1}{m_0} + \frac{P_2^2}{\hbar^2} \left(\frac{1}{E_g} + \frac{1}{E_g + 2\Delta_2} \right), \quad (13)$$

and Rashba coupling

$$\alpha_{\text{bulk}} = \frac{2P_2\Delta_{sz}}{(E_g + 2\Delta_2)} + \frac{4P_2\Delta_3^2\Delta_{sz}}{(E_g + 2\Delta_2)^2(E_g + \Delta_1 + \Delta_2)} - \frac{8P_2\Delta_{sz}^3}{(E_g + 2\Delta_2)^3}. \quad (14)$$

Note indeed that $\alpha_{\text{bulk}} \propto \Delta_{sz}$, which is finite only due to the broken cubic symmetry of the wurtzite crystal that allows for the s - p_z mixing.

3. CC basis: strained case

The application of an external stress on a bulk semiconductor leads to a shift of the energy levels and/or a splitting of the heavy-light holes degeneracy [52]. We discuss now, how strain effects change the band edges of the $k \cdot p$ Hamiltonian in Eq. (7).

We restrict ourselves to the case of biaxial strain, i.e.,

$$\begin{aligned} \varepsilon_{xx} &= \varepsilon_{yy} \neq \varepsilon_{zz} \\ \varepsilon_{xy} &= \varepsilon_{yz} = \varepsilon_{zx} = 0, \end{aligned} \quad (15)$$

where ε_{ij} ($i, j = x, y, z$) is the strain tensor. Notice that strain appearing in heterostructures is in general caused by a lattice mismatch at the interfaces. For a strained-layer wurtzite crystal pseudomorphically grown along the z direction, the components of the strain tensor assume the following values: $\varepsilon_{xx} = \varepsilon_{yy} = (a_s - a)/a$ and $\varepsilon_{zz} = -2C_{13}\varepsilon_{xx}/C_{33}$, where a_s is the lattice constant of the substrate and a of the epitaxy layer. The parameters C_{13} and C_{33} are the elastic stiffness constants [44, 56–58].

The conduction band edge has a hydrostatic energy shift given by $\Delta E_e = a_{c_1}\varepsilon_{zz} + a_{c_2}(\varepsilon_{xx} + \varepsilon_{yy})$, with $a_{c_1(c_2)}$ the conduction band deformation potential. The topmost A valence band edge shifts according to $\Delta E_A = S_1 + S_2$, where S_1 and S_2 are written as $S_1 = D_1\varepsilon_{zz} + D_2(\varepsilon_{xx} + \varepsilon_{yy})$ and $S_2 = D_3\varepsilon_{zz} + D_4(\varepsilon_{xx} + \varepsilon_{yy})$, with D_{1-4} the valence band deformation potentials [44, 59]. Therefore, the band gap variation, i.e., $\Delta E_g = E_g^s - E_g$, is given by $\Delta E_e - \Delta E_A$, with the superscript “s” denoting parameters in the strained case. The energy differences between valence bands read

$$E_{AB}^s = E_{AB} = 2\Delta_2, \quad (16)$$

$$E_{AC}^s = E_{AC} + S_2 = \Delta_1 + \Delta_2 + S_2, \quad (17)$$

where one can explicitly see the band edge corrections due to the deformation potentials [cf. Eqs. (9), (16), and (17)].

In Fig. 1(a) we show the diagonal matrix elements for both cases: unstrained (solid curves) and strained (dashed curves). Here, the only effect caused by strain is a shift in the band edges; one can then straightforwardly write down the corresponding Kane Hamiltonian by simply replacing E_g , E_{AB} , and E_{AC} in Eq. (7) by E_g^s , E_{AB}^s , and E_{AC}^s , respectively.

4. Some remarks

The Kane model in Eq. (7) was constructed including only the lowest conduction and top valence bands (see Table I). This model only provides a good description of the electronic states in the conduction band. In order to properly describe holes, especially heavy and light holes, it is necessary to include additional bands [51]. Nevertheless, here we are just interested in the conduction band. From Eqs. (12) and (13), for instance, we can calculate the longitudinal and transversal electronic effective masses, respectively, which, as we shall see in Sec. V, are in excellent agreement with experimental results.

We also derive a Kane Hamiltonian using the “diagonal basis”, in which the 8×8 matrix is diagonal at $k = 0$ (see Appendix B). This helps us determine the diagonal elements (not actual band edge energies) of the Kane model in the CC basis, as well as the corresponding “virtual” band offsets (see Table II) to correctly describe heterostructures. Note, though, that the diagonal basis has a direct dependence on the band parameters.

C. 8×8 Kane model: heterostructures

We shall focus now on the Kane model for wurtzite heterostructures, more specifically quantum wells grown along the z || (0001) direction (c axis), for which experimental data are available. Later on, we show a general formulation valid for wells, as well as wires and dots [see Sec. III B].

Due to the different band edges at $\mathbf{k} = 0$ for different materials, a sharp jump of the bands (offsets) happens at the interfaces, which introduces position-dependent potentials representing the different layers. For simplicity, we refer here to the unstrained case; the generalization to the strained case is straightforward (see Sec. II B 3).

1. Unstrained quantum wells

The Hamiltonian for wells looks exactly the same as that in Eq. (7), except that now one has to replace $k_z \rightarrow -i(\partial/\partial z)$, and introduce in the diagonal z -dependent potentials to account for the band offsets. Note that the diagonal basis functions depend on the band parameters (see Table IV in Appendix B), and hence, have different values on the well and on the barriers. This may lead to unnecessary complications in practice [60]. For convenience, we only consider the 8×8 Kane model for wells written in the CC basis. We emphasize that, strictly speaking, even in the CC basis set, the basis functions are z -dependent, as the periodic part of the Bloch functions, i.e., S , X , Y and Z , see Table I, can be different for the several layers. Here we neglect this difference, as it is usually done for zincblende heterostructures [60, 61].

Let us first analyze the z -dependent structural potential added to the diagonal part of Hamiltonian (7), for both the conduction and valence bands. From Fig. 1(b), where we schematically show the band offsets, we can straightforwardly obtain

$$V_{w-e}(z) = \delta_e h_w(z), \quad V_{w-i}(z) = -\delta_i h_w(z), \quad i \in \{A, B, C\}, \quad (18)$$

where $h_w(z) = \Theta(z - \frac{L_w}{2}) + \Theta(-z - \frac{L_w}{2})$ describes a dimensionless square well profile, with $\Theta(z)$ the Heaviside function. In this expression, the center of the well has been taken as the origin in the z direction ($z = 0$).

Once again, in addition to the z -dependent potentials in (18), the off-diagonal elements Δ_3 , Δ_{sz} , and the Kane parameters P_1 and P_2 should be z -dependent, since in principle they may have distinct values in different layers. In most wurtzite materials, though, they have very similar values [58], and from now on, we use them as z -independent parameters.

The discussion above on the Kane Hamiltonian for a quantum well is based on the single-electron picture, in which the electrons experience only the structural potential of the well. Below we focus on modulation doped quantum wells in the Hartree approximation. In this case, besides the structural well potential, the doping (from dopants) potential, the pure electron Hartree (from electrons) potential, as well as the external gate potential also contribute to the total electron potential.

2. Strained quantum wells

For strained wurtzite heterostructures, an internal potential (built-in electric field), due to the strain-induced piezoelectric polarization and/or spontaneous polarization, usually plays a significant role as well [62]. To calculate the built-in fields, two types of boundary conditions are usually used: (i) periodic boundary conditions, i.e., the potentials of the external surfaces are equal, and (ii) neutral external surfaces [63, 64]. The corresponding expressions for the electric fields E_w (well) and E_b (barriers) in both cases are given by

(i) periodic boundary conditions

$$E_w = \frac{2L_b(P_b - P_w)}{\epsilon_0 \epsilon_r (L_w + 2L_b)}, \quad E_b = E_w + \frac{P_w - P_b}{\epsilon_0 \epsilon_r}, \quad (19)$$

(ii) neutral external surfaces

$$E_w = \frac{P_b - P_w}{\epsilon_0 \epsilon_r}, \quad E_b = 0, \quad (20)$$

where ϵ_0 is the vacuum permittivity and P_w and P_b are the polarization fields (spontaneous and piezoelectric) appearing in the well and barriers, respectively. Here we have assumed a uniform dielectric constant ϵ_r throughout the system. Note that, as the width of the barriers goes to infinity, the two types of boundary conditions become equivalent.

The direction and magnitude of the spontaneous polarization along the c axis of a wurtzite crystal can be determined experimentally [62, 65, 66]. On the other hand, the magnitude of the piezoelectric polarization reads

$$P = 2 \frac{a_s - a}{a} \left(e_{31} - e_{33} \frac{C_{13}}{C_{33}} \right), \quad (21)$$

where e_{31} and e_{33} are piezoelectric coefficients. Both polarizations are calculated for the well and also for the barrier.

3. Total potential

The total self-consistent conduction and valence band potentials $V_e(z)$ and $V_i(z)$, $i \in \{A, B, C\}$, respectively, in strained wurtzite quantum wells are given by

$$V_e(z) = V_H(z) + V_{w-e}(z), \quad V_i(z) = V_H(z) + V_{w-i}(z), \quad (22)$$

with V_H the Hartree potential, which also has several contributions, namely,

$$V_H(z) = V_{\text{elect}}(z) + V_d(z) + V_{\text{int}}(z) + V_g(z), \quad (23)$$

where V_{elect} is the pure electron Hartree potential, V_d is the doping potential, V_{int} is the internal potential (due to the built-in electric field), and V_g is the external gate potential (see Appendix E for details).

III. EFFECTIVE 3D HAMILTONIAN

Based on the 8×8 Kane model for wurzite quantum wells discussed in the last section, we now derive an effective 2×2 Hamiltonian for the conduction band. To this end we can either use the Löwdin partitioning method, discussed in detail in Refs. [16, 45], or the folding down approach, shown in Appendix C. We use both approaches and obtain the same result. We also derive the effective model for wells using the theory of invariants, as shown in Appendix A 1.

A. Quantum well

Via Löwdin perturbation theory (or the folding down approach), we obtain the following effective 2×2 Hamiltonian for wurzite wells

$$\mathcal{H}^{3D} = \mathcal{H}_{qw} + \mathcal{H}_{so}^R + \mathcal{H}_{so}^D, \quad (24)$$

where the first contribution is spin-independent and the last two terms correspond to the Rashba and Dresselhaus SO interactions, respectively. The spin independent part is given by

$$\mathcal{H}_{qw}(z) = -\frac{\hbar^2}{2} \frac{d}{dz} \frac{1}{m_{\perp}(z)} \frac{d}{dz} + \frac{\hbar^2 k_{\parallel}^2}{2m_{\parallel}(z)} + V_{\text{eff}}(z) + V_e(z), \quad (25)$$

with m_{\perp} and m_{\parallel} the longitudinal and transversal effective masses, respectively,

$$\frac{1}{m_{\perp}(z)} = \frac{1}{m_0} + \frac{2P_1^2}{\hbar^2} \left[\frac{1}{E_g + \Delta_1 + \Delta_2} - \frac{V_e(z) - V_C(z)}{(E_g + \Delta_1 + \Delta_2)^2} \right], \quad (26)$$

$$\frac{1}{m_{\parallel}(z)} = \frac{1}{m_0} + \frac{P_2^2}{\hbar^2} \left[\frac{1}{E_g} + \frac{1}{E_g + 2\Delta_2} - \frac{V_e(z) - V_A(z)}{E_g^2} - \frac{V_e(z) - V_B(z)}{(E_g + 2\Delta_2)^2} \right]. \quad (27)$$

The extra effective potential $V_{\text{eff}} = V_D + V_s$ includes the Darwin term V_D and an s - p_z mixing-induced contribution V_s . The corresponding expressions read

$$V_D(z) = \frac{P_1^2}{2(E_g + \Delta_1 + \Delta_2)^2} \frac{d^2 V_e(z)}{dz^2}, \quad (28)$$

$$V_s(z) = \frac{2\Delta_{sz}^2}{E_g + 2\Delta_2} - \frac{2\Delta_{sz}^2 [V_e(z) - V_B(z)]}{(E_g + 2\Delta_2)^2}. \quad (29)$$

The spin-dependent Rashba Hamiltonian is given by

$$\mathcal{H}_{so}^R = \eta(z) (\sigma_x k_y - \sigma_y k_x), \quad (30)$$

with SO coupling parameter

$$\eta(z) = \eta_c(z) + \eta_H \frac{dV_H(z)}{dz} + \eta_w \frac{dV_{w-e}(z)}{dz}. \quad (31)$$

In the expression above, each term corresponds to the bulk, Hartree, and structural contributions, respectively.

The bulk Rashba contribution, due to both the well and barrier layers, reads

$$\eta_c(z) = \frac{2P_2\Delta_{sz}}{E_g + 2\Delta_2} \left[1 + \frac{4\Delta_3^2}{(E_g + \Delta_2)(E_g + \Delta_1 + \Delta_2)} - \frac{8\Delta_{sz}^2}{(E_g + 2\Delta_2)^2} - \frac{V_e(z) - V_B(z)}{E_g + 2\Delta_2} \right]. \quad (32)$$

Note that $\eta_c(z)$ takes different values in each layer, i.e., $\eta_c(|z| < L_w/2) \equiv \alpha_{\text{bulk}}(\text{well})$ [see Eq. (14)] and $\eta_c(|z| > L_w/2) \equiv \alpha_{\text{bulk}}(\text{barrier})$ [67]. We should emphasize that there is no analogue of such a contribution to the SO interaction in zincblende systems, in which the s - p_z mixing is not allowed by symmetry.

The Hartree and structural terms contribute only in third-order in the energy denominator,

$$\eta_H = \frac{P_1 P_2 \Delta_3}{(E_g + 2\Delta_2)(E_g + \Delta_1 + \Delta_2)} \left(\frac{1}{E_g + 2\Delta_2} + \frac{1}{E_g + \Delta_1 + \Delta_2} \right) \quad (33)$$

and

$$\eta_w = -\frac{P_1 P_2 \Delta_3}{(E_g + 2\Delta_2)(E_g + \Delta_1 + \Delta_2)} \left(\frac{\delta_C/\delta_e}{E_g + 2\Delta_2} + \frac{\delta_B/\delta_e}{E_g + \Delta_1 + \Delta_2} \right). \quad (34)$$

The Dresselhaus term, which in this case has the same symmetry as the Rashba, reads

$$\mathcal{H}_{so}^D = \gamma (bk_z^2 - k_{\parallel}^2) (\sigma_x k_y - \sigma_y k_x), \quad (35)$$

with γ and b determined in terms of bulk quantities, for details see Appendix D.

The expressions shown above for the Rashba coupling do not account for possible $\mathbf{k} \cdot \mathbf{p}$ terms within the valence band subspace. These are rigorously nonzero by point-group symmetry arguments [68, 69]. It can be shown, however, that their contribution is negligible. In Appendix D, we obtain the corresponding expression of H_v (valence band subspace) including the $\mathbf{k} \cdot \mathbf{p}$ interaction within the valence bands, characterized by the parameter $Q = -(i\hbar/m_0) \langle Z' | p_x | X \rangle = (i\hbar/m_0) \langle Z' | p_y | Y \rangle$. The additional terms in the 2×2 electron Hamiltonian are also derived, and we confirm their negligible effect on the Rashba SO coupling. This $\mathbf{k} \cdot \mathbf{p}$ interaction contributes to the Dresselhaus SO coupling as well. Though, we emphasize that in our simulations the Dresselhaus interaction is put by hand by treating the bulk Dresselhaus coefficients as semi-empirical parameters.

B. General expression

For completeness, we present below the general effective Schrödinger equation for electrons in wurzite heterostructures with an arbitrary confining potential and external magnetic field. More specifically, our general result is valid for quantum wells, wires, and dots [cf. Eq. (6.26) in Ref. [16] for zincblende heterostructures].

The total 2×2 Hamiltonian reads

$$H_{\text{eff}} = H_0 + \boldsymbol{\sigma} \cdot \mathbf{B}_{\text{eff}}(\mathbf{r}) + H_{\text{so}}, \quad (36)$$

in which H_0 is spin-independent, $\mathbf{B}_{\text{eff}}(\mathbf{r})$ is an effective mag-

netic field, and H_{so} is the SO coupling. The expression for H_0 is given by

$$H_0 = \frac{\hbar^2}{2} \left[\mathbf{k}_{\parallel} \frac{1}{m_{\parallel}(\mathbf{r})} \mathbf{k}_{\parallel} + \mathbf{k}_z \frac{1}{m_{\perp}(\mathbf{r})} \mathbf{k}_z \right] + V_e(\mathbf{r}) + \frac{2\Delta_{sz}^2}{E_g + 2\Delta_2} \left[1 - \frac{V_e(\mathbf{r}) - V_B(\mathbf{r})}{E_g + 2\Delta_2} \right] + \frac{P_1^2}{(E_g + \Delta_1 + \Delta_2)^2} \frac{\partial^2 V_e(\mathbf{r})}{\partial z^2} + \left[\frac{P_2^2}{E_g^2} + \frac{P_2^2}{(E_g + 2\Delta_2)^2} \right] \nabla_{\parallel}^2 V_e(\mathbf{r}), \quad (37)$$

where the out-of-plane and in-plane effective masses, which now that depend on \mathbf{r} , are given by Eqs. (26) and (27), respec-

tively. The last two terms in (37) are equivalent to the Darwin term in the Pauli equation [70].

The effective magnetic field can be written as

$$\mathbf{B}_{\text{eff}}(\mathbf{r}) = -\frac{e}{\hbar} \frac{P_1 P_2 \Delta_3}{(E_g + \Delta_2)(E_g + \Delta_1 + \Delta_2)} \left(1 - \frac{V_e(\mathbf{r}) - V_B(\mathbf{r})}{E_g + 2\Delta_2} + \frac{V_e(\mathbf{r}) - V_C(\mathbf{r})}{E_g + \Delta_1 + \Delta_2} \right) (B_x \hat{x} + B_y \hat{y}) + \frac{e}{\hbar} \frac{P_2^2}{2} \left(-\frac{V_A(\mathbf{r})}{E_g^2} + \frac{V_B(\mathbf{r})}{(E_g + 2\Delta_2)^2} \right) B_z \hat{z}, \quad (38)$$

where $\mathbf{B} = \sum_{i=x,y,z} B_i \hat{i}$ is the applied magnetic field. The SO

Hamiltonian reads

$$H_{\text{so}} = \left(\frac{2P_2\Delta_{sz}}{E_g + 2\Delta_2} + \frac{4P_2\Delta_3^2\Delta_{sz}}{(E_g + 2\Delta_2)^2(E_g + \Delta_1 + \Delta_2)} - \frac{8P_2\Delta_{sz}^3}{(E_g + 2\Delta_2)^3} \right) (\sigma_x k_y - \sigma_y k_x) - \frac{P_2\Delta_{sz}}{(E_g + 2\Delta_2)^2} \{ \sigma_x k_y - \sigma_y k_x, V_e(\mathbf{r}) - V_B(\mathbf{r}) \} + \frac{P_2^2}{2E_g^2} [\mathbf{k} \times \nabla V_A(\mathbf{r})]_z \sigma_z - \frac{P_2^2}{2(E_g + \Delta_2)^2} [\mathbf{k} \times \nabla V_B(\mathbf{r})]_z \sigma_z + \frac{P_1 P_2 \Delta_3}{(E_g + 2\Delta_2)^2 (E_g + \Delta_1 + \Delta_2)} \boldsymbol{\sigma}_{\parallel} \cdot [\mathbf{k} \times \nabla V_B(\mathbf{r})]_{\parallel} + \frac{P_1 P_2 \Delta_3}{(E_g + 2\Delta_2)(E_g + \Delta_1 + \Delta_2)^2} \boldsymbol{\sigma}_{\parallel} \cdot [\mathbf{k} \times \nabla V_C(\mathbf{r})]_{\parallel} + \frac{P_2\Delta_{sz}}{(E_g + 2\Delta_2)^3} \{ \sigma_x k_y - \sigma_y k_x, V_e^2(\mathbf{r}) + V_B^2(\mathbf{r}) \} - \frac{P_2\Delta_{sz}}{(E_g + 2\Delta_2)^3} \left[\{ V_e(\mathbf{r}), (\sigma_x k_y - \sigma_y k_x) V_B(\mathbf{r}) \} + \{ V_B(\mathbf{r}), (\sigma_x k_y - \sigma_y k_x) V_e(\mathbf{r}) \} \right], \quad (39)$$

with \mathbf{k} the kinetic momentum, i.e., $\hbar\mathbf{k} = -i\hbar\nabla + e\mathbf{A}$, $\mathbf{B} = \nabla \times \mathbf{A}$ (real external field), which should be distinguished from the canonical momentum $\hbar\mathbf{k} = -i\hbar\nabla$. The bracket $\{ \cdot, \cdot \}$ stands for the anti-commutator.

The general Hamiltonian in Eq. (36) is one of the main results of the present paper. We must point out a major difference between the latter and the effective model for zincblende structures [16]: the nonequivalence between the z direction with respect to x and y allows for the s - p_z hybridization, which then leads to the emergence of additional terms (see coefficients $\propto \Delta_{sz}$).

From the expressions above, it is quite simple to see this nonequivalence between z and x, y . For the sake of simplicity, let us focus on the bulk case. In addition to having differ-

ent effective masses in the longitudinal and transversal directions [see Eqs. (12) and (13), respectively], Eq. (38) reveals an anisotropy in the effective g -factor, there is no z -component. This feature, as well as the analysis of the extra terms mentioned above, will be addressed elsewhere.

Note that, apart from the Dresselhaus term (not included in the derivation above), Eq. (24) is a particular case of (36), see Eqs. (25)–(34).

Our general Hamiltonian can be used to study a variety of heterostructures. Next we focus on one- and two-subband quantum wells, for which we can write down an effective Hamiltonian and self-consistently determine all the relevant SO couplings.

IV. EFFECTIVE 4×4 HAMILTONIAN

From the 3D Hamiltonian of Sec. III A, we can derive an effective low-energy quasi-2D model. More specifically, here we obtain a model Hamiltonian for quantum wells with one and two subbands.

Our approach consists first of self-consistently determining the spin-degenerate eigenvalues $\mathcal{E}_{k_{\parallel\nu}} = \mathcal{E}_{\nu} + \hbar^2 k_{\parallel}^2 / 2m_{\parallel}$ and

$$\mathcal{H}^{2D} = \begin{pmatrix} \mathcal{E}_{k_{\parallel 1}} & i(\alpha_1 + \beta_1)k_- & 0 & i(\eta + \Gamma)k_- \\ -i(\alpha_1 + \beta_1)k_+ & \mathcal{E}_{k_{\parallel 1}} & -i(\eta + \Gamma)k_+ & 0 \\ 0 & i(\eta + \Gamma)k_- & \mathcal{E}_{k_{\parallel 2}} & i(\alpha_2 + \beta_2)k_- \\ -i(\eta + \Gamma)k_+ & 0 & -i(\alpha_2 + \beta_2)k_+ & \mathcal{E}_{k_{\parallel 2}} \end{pmatrix}. \quad (40)$$

Here we have neglected the z -dependence of m_{\parallel} and chosen its value in the well layer since the electrons are mostly confined there. In Sec. V A, we evaluate m_{\parallel} and show it is in great agreement with experimental results.

The two 2×2 blocks [upper left (α_1, β_1) and lower right (α_2, β_2)] of Eq. (40) correspond to the usual Rashba-Dresselhaus Hamiltonian coupled by the ‘‘off-diagonal’’ intersubband block (η, Γ) . Note, however, that differently from zincblende materials, the Rashba and Dresselhaus terms have the same symmetry.

The intrasubband (intersubband) Rashba α_{ν} (η) and Dresselhaus β_{ν} (Γ) SO coefficients are defined as follows

$$\eta_{\nu\nu'} = \langle \psi_{\nu} | \eta_c(z) + \eta_H \partial_z V_H(z) + \eta_w \partial_z V_{w-e}(z) | \psi_{\nu'} \rangle, \quad (41)$$

and

$$\Gamma_{\nu\nu'} = \gamma (b \langle \psi_{\nu} | k_z^2 | \psi_{\nu'} \rangle - k_{\parallel}^2 \delta_{\nu\nu'}), \quad (42)$$

where the Rashba coefficients are $\alpha_{\nu} \equiv \eta_{\nu\nu}$, within each subband, and $\eta \equiv \eta_{12}$, between subbands. The same is valid for the Dresselhaus coefficients $\beta_{\nu} \equiv \Gamma_{\nu\nu}$ and $\Gamma \equiv \Gamma_{12}$.

The Rashba coupling α_{ν} (η) can be written in terms of several contributions, i.e., $\alpha_{\nu} = \alpha_{\nu}^c + \alpha_{\nu}^H + \alpha_{\nu}^w$, being $\alpha_{\nu}^c = \langle \psi_{\nu} | \eta_c(z) | \psi_{\nu} \rangle$ the bulk coefficient [49], $\alpha_{\nu}^H = \eta_H \langle \psi_{\nu} | \partial_z V_H(z) | \psi_{\nu} \rangle$ the Hartree term, and $\alpha_{\nu}^w = \eta_w \langle \psi_{\nu} | \partial_z V_{w-e}(z) | \psi_{\nu} \rangle$ the contribution due to the structural potential. The Hartree coefficient can also be split into different contributions [see Eq. (23)],

$$\alpha_{\nu}^H = \alpha_{\nu}^{\text{elect}} + \alpha_{\nu}^d + \alpha_{\nu}^{\text{int}} + \alpha_{\nu}^g, \quad (43)$$

where

$$\alpha_{\nu}^{\text{elect}} = \eta_H \langle \psi_{\nu} | \partial_z V_{\text{elect}}(z) | \psi_{\nu} \rangle, \quad (44)$$

$$\alpha_{\nu}^d = \eta_H \langle \psi_{\nu} | \partial_z V_d(z) | \psi_{\nu} \rangle, \quad (45)$$

$$\alpha_{\nu}^{\text{int}} = \eta_H \langle \psi_{\nu} | \partial_z V_{\text{int}}(z) | \psi_{\nu} \rangle, \quad (46)$$

and

$$\alpha_{\nu}^g = \eta_H \langle \psi_{\nu} | \partial_z V_g(z) | \psi_{\nu} \rangle \quad (47)$$

corresponding eigenspinors $|\mathbf{k}_{\parallel\nu\sigma}\rangle = |\mathbf{k}_{\parallel\nu}\rangle \otimes |\sigma\rangle$, $\langle \mathbf{r} | \mathbf{k}_{\parallel\nu}\rangle = e^{i\mathbf{k}_{\parallel\nu} \cdot \mathbf{r}_{\parallel}} \psi_{\nu}(z)$ of H_{qw} (25). Here \mathcal{E}_{ν} (ψ_{ν}) is the ν^{th} subband (wave function) of the well and $\sigma = \uparrow, \downarrow$ is the electron spin component along the z direction. Then we project the total 3D Hamiltonian (24) onto the basis set $\{|\mathbf{k}_{\parallel\nu\sigma}\rangle\}$.

Explicitly, the effective model with two subbands $\{|\mathbf{k}_{\parallel 1} \uparrow\rangle, |\mathbf{k}_{\parallel 1} \downarrow\rangle, |\mathbf{k}_{\parallel 2} \uparrow\rangle, |\mathbf{k}_{\parallel 2} \downarrow\rangle\}$, in the coordinate system $x|| (100)$, $y|| (010)$, can be written as

are due to, respectively, the purely electron Hartree potential, the doping potential, the internal potential (built-in electric fields), and the external gate potential. Note that all these SO coupling coefficients depend on the self-consistent potential and the subband wave functions.

Interestingly, as mentioned above, the Rashba and Dresselhaus terms induce the same electron spin configuration in a c axis oriented wurtzite structure [71, 72], in contrast to the (001)-grown zincblende heterostructures. This allows us to define an effective SO coupling parameter for each subband $\alpha_{\nu}^{\text{eff}} = \alpha_{\nu} + \beta_{\nu}$, and similarly an effective intersubband SO term $\eta^{\text{eff}} = \eta + \Gamma$. Therefore, experimental measurements of the SO splittings correspond to the effective coupling coefficients $\alpha_{\nu}^{\text{eff}}$ and η^{eff} . In the following, we evaluate these quantities by self-consistently solving Schrödinger and Poisson equations.

V. RESULTS AND DISCUSSIONS

Here we first introduce the structure of the wells. Then we discuss our calculated SO couplings based on the model presented in the previous sections. Our discussions cover both the single and double well cases with either one or two occupied subbands.

A. Heterostructures

We consider GaN/Al_xGa_{1-x}N heterostructures grown along the $z|| [0001]$ direction. For the single-well, our heterostructure is defined by a well of width $L_w = 10$ nm and two symmetric barrier regions of width $L_b = 7$ nm [see Fig. 1(b)]. Unless otherwise stated, the electron density is *fixed* at $n_e = 1.0 \times 10^{12}$ cm⁻², arising from two symmetrically doped layers sitting 6 nm away from the center of the well. Our double well has a similar geometry, except for an additional barrier of width $L_{cb} = 2$ nm embedded in the center of the structure.

Wurtzite GaN-based heterostructures are usually grown on a GaN substrate by molecular beam epitaxy, i.e., the Al_xGa_{1-x}N barriers are deformed and the corresponding lat-

tice constant is adjusted to the GaN substrate and quantum wells [64, 73, 74], which is the case we consider here. In the $\text{Al}_x\text{Ga}_{1-x}\text{N}$ layers [58], we choose the SO and the crystal field splitting parameters $\Delta_{\text{so}} = 0.014$ eV, $\Delta_{\text{cr}} = 0.019 - 0.183x$ eV, respectively, the lattice constant $A_l = 3.189 - 0.077x$ Å, the deformation potentials $D_1 = -3.0$ eV, $D_2 = 3.6$ eV, $D_3 = 8.82 + 0.78x$ eV, $D_4 = -4.41 + 0.39x$ eV (valence band), $a_{c1} = -9.5 - 2.5x$ eV, $a_{c2} = -8.2 + 2.8x$ eV (conduction band) [59], and the elastic constants $C_{13} = 106 + 2x$ Gpa, $C_{33} = 398 - 25x$ Gpa [75]. The unstrained band gap is $E_g = 3.507 + 2.723x$ eV and the strained one is calculated by taking into account the strain-induced band edge shifts [see Sec. II B 3]. The spontaneous polarization is given by $-0.029 - 0.051x$ C·m⁻² and the piezoelectric coefficients by $e_{13} = -0.35 - 0.15x$ C·m⁻², $e_{33} = 1.27 + 0.25x$ C·m⁻² [58].

Table II. Band parameters (in eV) for GaN/ $\text{Al}_x\text{Ga}_{1-x}\text{N}$ heterostructures, see the single well shown in Fig. 1(b).

x	$\delta_e(\delta_{be})$	$\delta_g(\delta_{bA})$	$\delta_B(\delta_{bB})$	$\delta_C(\delta_{bC})$
0.30	0.5252	0.2950	0.1546	0.2784
0.40	0.7051	0.4044	0.2098	0.3877
0.50	0.8876	0.5157	0.2059	0.4990
0.60	1.0728	0.6288	0.3228	0.6120
0.70	1.2608	0.7438	0.3805	0.7270
0.80	1.4515	0.8606	0.4391	0.8438

The fraction of the s - p_z mixing we consider here is of $\sim 1\%$. This is the same value used for ZnO, which has a very similar band gap. We then obtain $\Delta_{\text{sz}} \sim 0.467$ meV [35, 76]. The interband Kane parameters are taken as $E_1 = E_2 = 14.0$ eV [58, 77–79], with $E_{1,2} = 2m_0P_{1,2}^2/\hbar^2$, and are assumed the same in the well and barriers. We choose a uniform dielectric constant $\epsilon_r = 10.0$ [80] and consider the temperature $T = 2$ K. The relevant band parameters for GaN/ $\text{Al}_x\text{Ga}_{1-x}\text{N}$ heterostructures are shown in Table II for typical Al contents on the barriers [see Fig. 1(b)].

By inserting the relevant parameters listed above into Eqs. (26) and (27), we self-consistently determine the out-of-plane $m_{\perp}(\text{GaN}) = 0.2014m_0$ and in-plane $m_{\parallel}(\text{GaN}) = 0.2005m_0$ effective masses, in excellent agreement with the experimental values, $0.2m_0$ and $0.2m_0$ [58, 81], respectively. We also calculate the Rashba SO constants $\alpha_{\text{bulk}}(\text{GaN}) = 1.938$ meV·Å, $\eta_H = 0.01138$ Å², and $\eta_w = 2.462$ meV·Å², see Eqs. (32)–(34). For the Dresselhaus parameters γ and b [see Eq. (35)], we use $\gamma = 0.32$ eV·Å³ and $b = 3.855$ [23, 24].

B. Single well

Next we show our calculated SO coupling coefficients for a GaN/ $\text{Al}_{0.3}\text{Ga}_{0.6}\text{N}$ single well with one occupied subband. The dependence of these SO couplings on the Al content x on the $\text{Al}_x\text{Ga}_{1-x}\text{N}$ layers is discussed as well. We also determine the SO couplings of a GaN/ $\text{Al}_{0.3}\text{Ga}_{0.6}\text{N}$ well with two occupied subbands.

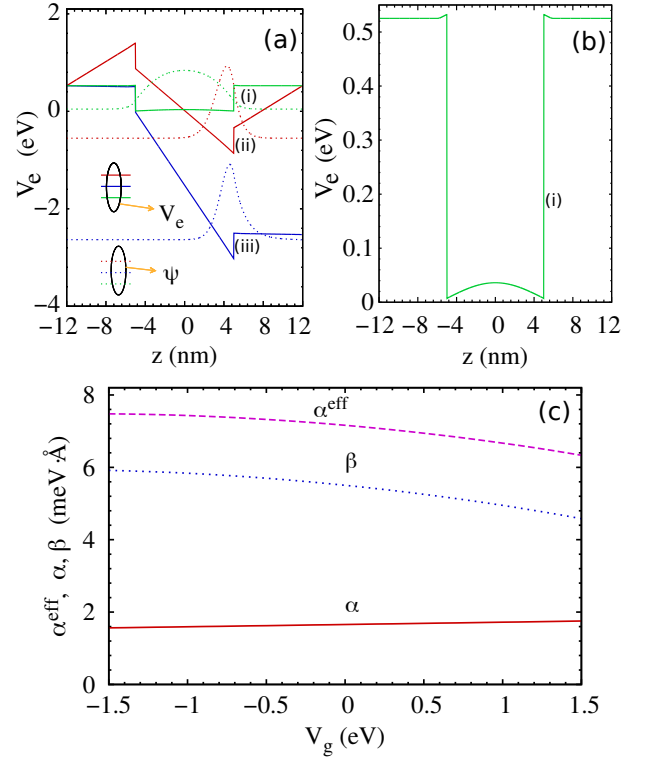


Figure 2. (Color online) (a) Self-consistent potential V_e (solid curves) and wave function profile ψ of the first subband (dotted curves) for three different conditions of the built-in fields, for a GaN/ $\text{Al}_{0.3}\text{Ga}_{0.7}\text{N}$ single well at $V_g = 0$. (i) green curves: zero built-in field (flat-band model); (ii) red curves: built-in field with periodic boundary conditions; (iii) blue curves: built-in field with neutral surface charge boundary conditions. The energy level (not shown) of the first subband for these three conditions are $E_1 = 44.9, -551.2, -2634.2$ meV, respectively. (b) Blowup of the potential V_e in the flat-band model. (c) Rashba α , Dresselhaus β , and effective SO $\alpha^{\text{eff}} = \alpha + \beta$ couplings as functions of V_g . The areal electron density is kept fixed at 1.0×10^{12} cm⁻², so that only the first subband is occupied. The temperature is $T = 2$ K.

1. One occupied subband

Before discussing the SO couplings in detail, let us first have a look at our self-consistent solutions. Figure 2(a) shows the profiles of the conduction band potential V_e and of the first subband wave function of a GaN/ $\text{Al}_{0.3}\text{Ga}_{0.7}\text{N}$ single well with only one occupied subband. We consider three cases: (i) the flat-band model (no built-in field) (green curves), (ii) periodic boundary conditions (red curves), and (iii) neutral surface charge boundary conditions (blue curves).

We observe that the flat-band model produces the usual profile of a confining square well potential [see Fig. 2(b)] and its corresponding envelope wave function. In contrast, in the presence of the strong built-in field (spontaneous and piezoelectric, \sim MV/cm [62, 78]), both the periodic and the neutral surface charge boundary conditions transform the rectangular-type well into a triangular-like one. Accordingly, electrons are mainly confined near one of the well/barrier interfaces.

We find that the SO couplings calculated in GaN wells in both cases are comparable, the discrepancy being of just ~ 0.2 meV $\cdot\text{\AA}$. Thus in the following, we focus on the widely adopted periodic boundary conditions [82, 83].

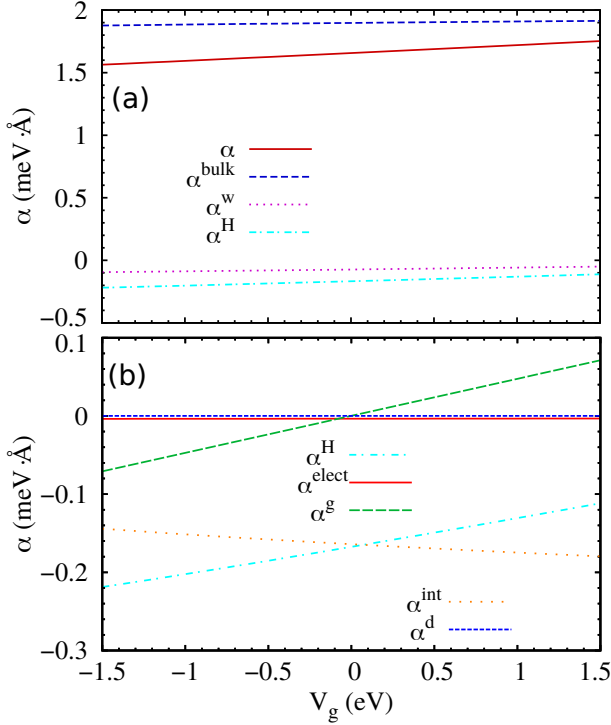


Figure 3. (Color online) (a) Rashba α and its several contributions: the bulk α_{bulk} , the structural α^w , and the Hartree α^H contributions as functions of V_g in a GaN/Al_{0.3}Ga_{0.7}N single well with one occupied subband. (b) Contributions to α^H : the pure electron Hartree α^{elect} , the internal field α^{int} , the doping α^d , and the external gate α^g coefficients as functions of V_g . The areal electron density is held fixed at $1.0 \times 10^{12} \text{cm}^{-2}$. The temperature is $T = 2$ K.

Figure 2(c) shows the Rashba α , Dresselhaus β , and effective SO $\alpha^{\text{eff}} = \alpha + \beta$ couplings as functions of the gate voltage V_g . One can see that the Rashba term is relatively weaker than the Dresselhaus coupling, but their magnitudes are comparable. At zero bias $V_g = 0$, we obtain the total SO coupling intensity $\alpha^{\text{eff}} = 7.16$ meV $\cdot\text{\AA}$, in agreement with results from weak antilocalization measurements, in which the spin splitting parameter was reported ranging from 5.5 to 10.01 meV $\cdot\text{\AA}$ [26–28, 30, 37]. In addition, we find that the Rashba coupling, which in general strongly depends on V_g in usual zincblende quantum wells, remains essentially constant as V_g varies. The weak dependence of α on V_g follows from the interplay of its several different contributions, as we discuss next.

In Fig. 3(a) we show each contribution of α as a function of V_g . Figure 3(b) further shows the several terms of α^H [see Eqs. (44)–(47)]. For the GaN and Al_{0.3}Ga_{0.7}N layers, we obtain $\alpha_{\text{bulk}}(\text{GaN}) = 1.938$ meV $\cdot\text{\AA}$ and $\alpha_{\text{bulk}}(\text{AlGa}) = 1.570$ meV $\cdot\text{\AA}$. Since the wave function is mostly confined in the well (GaN layer), the intrinsic bulk contribution $\alpha_{\text{bulk}} \approx \alpha_{\text{bulk}}(\text{GaN})$ remains essentially constant as V_g varies.

The combined contributions of the Hartree α^H and structural α^w terms refer to the usual Rashba coupling induced by the structural inversion asymmetry of the system. As can be seen in Figs. 3(a) and 3(b), the usual Rashba term is approximately one tenth of the bulk Rashba contribution. Therefore, the total Rashba coupling has a similar behavior with V_g as the bulk Rashba term, i.e., it is weakly gate-dependent. In available reports on the SO coupling in wurtzite heterostructures concerning $k \cdot p$ interactions, however, the bulk Rashba term was missed [36, 44, 46]. On the other hand, we must emphasize that, even though the usual Rashba term is much weaker than the bulk Rashba coupling in GaN-based wurtzite wells, its contribution in relatively narrow gap semiconductors (e.g., GaAs in the wurtzite phase) can become important, thus possibly leading to a sensitive electrical control of it.

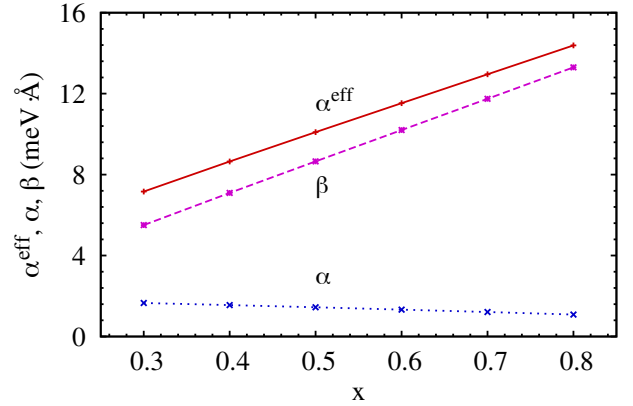


Figure 4. (Color online) Rashba α , Dresselhaus β , and the effective SO $\alpha^{\text{eff}} = \alpha + \beta$ strengths in GaN/Al_xGa_{1-x}N single wells with one occupied subband as functions of the Al content x at $V_g = 0$. The areal electron density n_e is held fixed at $1.0 \times 10^{12} \text{cm}^{-2}$. The temperature is $T = 2$ K.

Let us now consider the effects on the SO couplings of the Al content on the Al_xGa_{1-x}N layers. The Al x content modifies the strength of the built-in field and the band offsets of the well, consequently changing the SO couplings. Figure 4 shows α , β , and α^{eff} as functions of x at $V_g = 0$. We find that the Dresselhaus coupling β increases almost linearly with x . This is due to an increase of the piezoelectric polarization in the barriers as x varies, which makes the electrons more confined in the well. On the other hand, we observe that the Rashba term α is not sensitive to x , again because of the dominant bulk contribution.

2. Two occupied subbands

Here we change the doping conditions so we can effectively occupy the second subband. In contrast to the case of one occupied subband, in which we have two symmetrically doped layers, we have now only a one-side doping layer (asymmetric doping), so that the doping field can partially compensate the built-in field, thus making the well confinement profile less steep. In addition, we increase the areal electron density to $n_e = 1.5 \times 10^{13} \text{cm}^{-2}$. This corresponds to a higher doping

density n_d in the doping layer. Since we assume $n_d = n_e$, we ensure charge neutrality in our system.

Figure 5(a) shows the self-consistent confining potential V_e and the wave function profile of the first ψ_1 and second ψ_2 occupied subbands of the well at $V_g = 0$. Because of the change in the doping conditions, we observe that the well becomes flatter [cf. Figs. 2(a) and 5(a)]. In Fig. 5(b), we show the intrasubband Rashba α_v and Dresselhaus β_v , as well as the intersubband Rashba η and Dresselhaus Γ SO couplings as functions of V_g . The coupling α_v depends very weakly on V_g , similarly to the case of one occupied subband [cf. Figs. 2 and 5], because of the dominant contribution of the bulk Rashba term. The various constituents of α_v are not shown since they all have the same behavior as in the one occupied subband case.

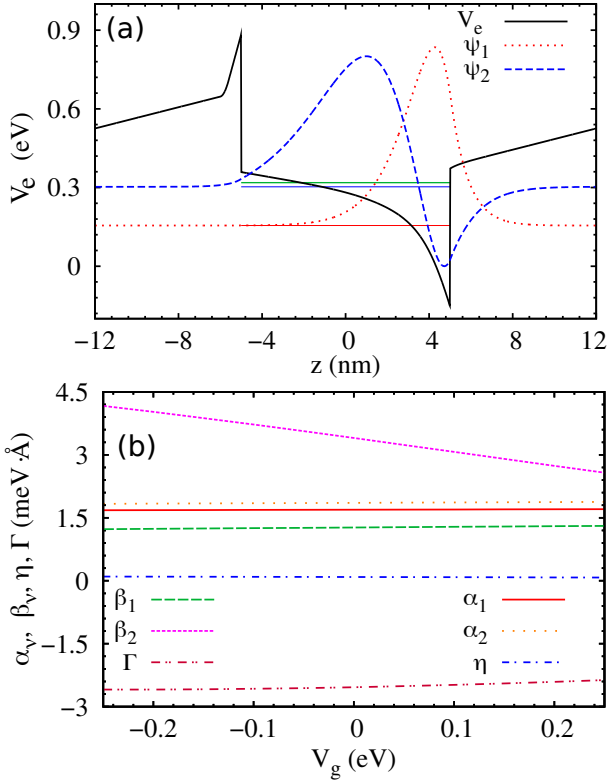


Figure 5. (Color online) (a) Self-consistent potential profile V_e and wave function profile of the first ψ_1 and second ψ_2 occupied subbands of a GaN/Al_{0.3}Ga_{0.7}N one-side doped single well at $V_g = 0$. The horizontal blue, red, and green lines inside the well indicate the subband energy levels $\mathcal{E}_1 = 155.1$ meV, $\mathcal{E}_2 = 302.8$ meV, and the Fermi level $\mathcal{E}_F = 318.5$ meV, respectively. (b) Intrasubband (intersubband) Rashba α_v (η) and Dresselhaus β_v (Γ) SO couplings as functions of V_g . The areal electron density is held fixed at $n_e = 1.5 \times 10^{13}$ cm⁻². The temperature is $T = 2$ K.

As for the coupling β_v , as the confining potential becomes flatter, we find that the first subband term β_1 is around four times weaker than that in the well with only one subband occupied. In addition, β_1 remains almost constant as V_g varies. On the other hand, for the second subband, β_2 is relatively sensitive to V_g . We attribute the different behaviors of β_1

and β_2 with V_g , to the distinct distributions of electrons occupying the first and second subbands. Electrons occupying the first subband are mostly confined to the right well/barrier interface (i.e., a narrow triangular confinement) [see ψ_1 in Fig. 5(a)], and cannot “feel” an overall modification of the potential due to V_g . However, electrons occupying the second band spread almost all over the whole well region [see ψ_2 in Fig. 5(a)]. Thus, the second subband wave function profile ψ_2 is more strongly dependent on V_g , further leading $\beta_2 = \gamma(b\langle\psi_2|k_z^2|\psi_2\rangle - k_{F,2}^2)$ to be more sensitive to V_g as compared to β_1 [see Fig. 5(b)]. Here $k_{F,v} = \sqrt{2\pi n_v}$ is the Fermi wave vector of the v th subband and n_v its occupation.

The intersubband Rashba coupling strength η is much weaker than the intrasubband coupling α_v . We attribute this to the fact that the bulk intersubband Rashba contribution $\eta_{\text{bulk}} = \langle\psi_1|\eta_c(z)|\psi_2\rangle$ to η is negligible, as electrons are mostly confined inside the well. More specifically, we have $\eta_{\text{bulk}} = \langle\psi_1|\eta_c(z)|\psi_2\rangle \approx \langle\psi_1|\alpha_{\text{bulk}}(\text{GaN})|\psi_2\rangle \sim 0$. Note that for α_v , the bulk term α_{bulk} dominates over the usual Rashba contributions. On the other hand, for the intersubband Dresselhaus term $\Gamma = \langle\psi_1|k_z^2|\psi_2\rangle$, we find that it is comparable to β_v . We should emphasize that Γ vanishes in the symmetric configuration because of parity. Here Γ is nonzero at $V_g = 0$, due to the presence of both the built-in field and the asymmetric one-side doping field.

C. Double well

In this section, we focus on obtaining the SO couplings for the double quantum well GaN/Al_{0.3}Ga_{0.7}N with an Al_xGa_{1-x}N central barrier (see Sec. V A).

Before discussing the SO couplings in detail, let us first have a look at how the Al content in the central barrier affects the double well configuration. At low Al concentration, we find that the electrons are mostly confined to one side [right side of our wells, see Fig. 6(a)] of the system, due to the presence of the strong built-in field, which makes the double well essentially an *effective* single well. Figure 6(a) shows the electron confining potential V_e and the wave function profiles ψ_v ($v = 1, 2$) of the lowest two subbands in a double well with $x = 0.3$ in the central barrier. Although only one subband is occupied in this configuration, for comparison, we also show ψ_2 for the empty second level of the well. As can be easily seen, this double-well configuration is essentially similar to the ones of the single wells discussed in previous sections.

If we further increase the Al content in the central barrier, we find that the left and right sides of the double well compete to confine the electrons. Interestingly, when $x \sim 0.69$, a *seemingly* symmetric configuration occurs. In Fig. 6(b), we show the corresponding confining potential and the wave function profiles at this configuration with two occupied subbands. We can see that the electrons occupying the two subbands are almost equally distributed on the left and right sides of the well, in contrast to the case of smaller values of x [cf. Figs. 6(a) and 6(b)]. However, we emphasize that this seemingly symmetric configuration (at $x = 0.69$) is actually structurally asymmetric, since the gradient of the potential (i.e., the electric field)

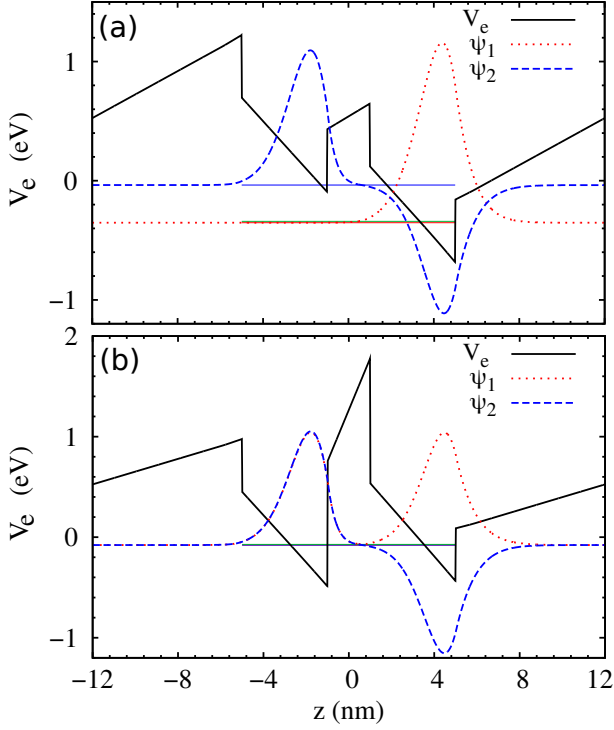


Figure 6. (Color online) Self-consistent potential V_e and wave function profiles ψ_ν ($\nu = 1, 2$) of a GaN/Al_{0.3}Ga_{0.7}N double well with an Al_{*x*}Ga_{1-*x*}N central barrier at $V_g = 0$. (a) One occupied subband with $x = 0.3$ in the central barrier; (b) two occupied subbands with $x = 0.69$ in the central barrier. For comparison, in (a) it is shown the second subband wave function ψ_2 for the empty second level. The horizontal blue, red, and green lines inside the well indicate the subband energy levels \mathcal{E}_1 , \mathcal{E}_2 , and the Fermi level \mathcal{E}_F , respectively. In (a), $\mathcal{E}_1 = -352.3$ meV, $\mathcal{E}_2 = -336.6$ meV, and $\mathcal{E}_F = -340.4$ meV; in (b), $\mathcal{E}_1 = -78.2$ meV, $\mathcal{E}_2 = -78.2$ meV, and $\mathcal{E}_F = -72.2$ meV. The areal electron density n_e is held fixed at $1.0 \times 10^{12} \text{ cm}^{-2}$.

has the same sign (negative) on the left and right wells, see Fig. 6(b). Next we determine the SO coupling coefficients for this configuration and discuss how these change with V_g .

Figure 7(a) shows $\alpha_\nu = \alpha_\nu^{\text{bulk}} + \alpha_\nu^{\text{H}} + \alpha_\nu^{\text{w+b}}$ and their several different contributions: α_ν^{bulk} , α_ν^{H} , and $\alpha_\nu^{\text{w+b}}$, with $\alpha_\nu^{\text{w+b}} \equiv \alpha_\nu^{\text{w}} + \alpha_\nu^{\text{b}}$, for each subband $\nu = 1, 2$. Note that the structural term in a double well has an additional contribution $\alpha_\nu^{\text{b}} = \eta_b \langle \nu | \frac{dV_b(z)}{dz} | \nu \rangle$ due to the presence of the central barrier [19]. The potential $V_b(z)$ describes the structural potential between the well and the central barrier. Straightforwardly, η_b has the same expression as η_w [see Eq. (31)] with the well offsets δ_i being replaced by the central barrier offsets δ_{bi} . Similarly to the case of single wells, we find that α_ν remains essentially constant as a function of V_g , since the bulk contribution (not sensitive to V_g) dominates over all the other contributions. Interestingly, we find that α_1 and α_2 almost interchange their respective values, across the seemingly symmetric configuration (at $V_g = 0$), because electrons occupying the first and second subbands interchange their distributions for $V_g > 0$ and $V_g < 0$. This feature of interchanging values across $V_g = 0$ also holds for the Dresselhaus terms β_1 and β_2 , with even more

pronounced behavior (cf. α_ν 's), as shown in Fig. 7(b).

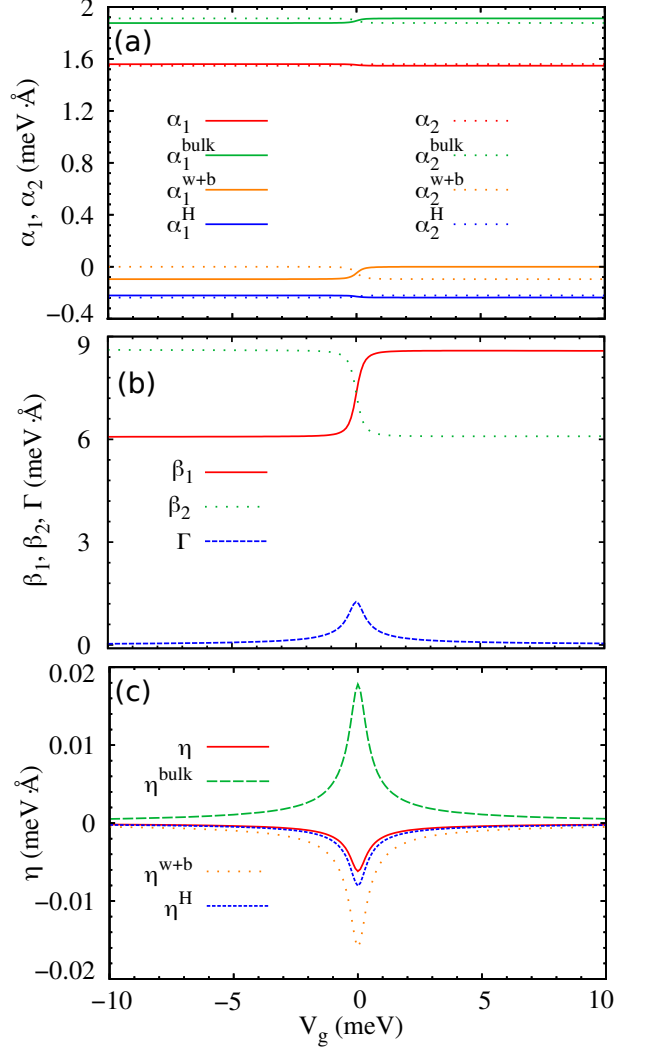


Figure 7. (Color online) (a) Intraband Rashba couplings α_ν ($\nu = 1, 2$) for a GaN/Al_{0.3}Ga_{0.7}N double well with an Al_{0.69}Ga_{0.31}N central barrier as functions of V_g . Several distinct constituents of α_ν : the bulk α_ν^{bulk} , the structural α_ν^{w} , and the total Hartree α_ν^{H} contributions. (b) Intraband β_ν and intersubband Γ Dresselhaus SO strengths as functions of V_g . (c) Intersubband η and its various contributions versus V_g . The areal electron density is held fixed at $1.0 \times 10^{12} \text{ cm}^{-2}$.

In Figs. 7(b) and 7(c), we show the intersubband Dresselhaus Γ and the Rashba η couplings, respectively, as functions of V_g . We find that both η and Γ achieve their maximal strength at $V_g = 0$, in contrast to the intraband α_ν and β_ν . This arises from the intersubband SO couplings depending on the overlap of the wave functions ψ_1 and ψ_2 of the two subbands, see Eqs. (41) and (42). At $V_g = 0$ (seemingly symmetric configuration), ψ_1 and ψ_2 have a perfect overlap. However, away from $V_g = 0$, ψ_1 and ψ_2 are largely separated, i.e., one is mostly confined in the left well and the other in the right well.

On the other hand, for large Al concentration in the central barrier ($x \sim 0.84$), we find that the one subband electron occupation is restored (for the same areal electron density),

similarly to the case of low x mentioned previously, except that we have an almost reversed configuration of the left and right wells constituting the double well structure.

VI. CONCLUDING REMARKS

We have derived a very general SO Hamiltonian for conduction electrons in wurtzite heterostructures valid for arbitrary confining potentials (quantum wells, wires, and dots) and external magnetic fields. Our starting point is the 8×8 Kane model including the s - p_z orbital mixing relevant to wurtzite systems. We then obtain a 2×2 effective SO Hamiltonian by applying both the Lwdin perturbation theory and the folding down approach. For concreteness, we focus on GaN/AlGaN wells and investigate in detail the electron SO couplings.

In addition to the s - p_z orbital mixing (absent in zincblende structures), we have taken into account the renormalization of the conduction band spinor component when deriving the effective 2×2 electron Hamiltonian for heterostructures; these two elements were not included in previous works. Most importantly, we find that these are crucial in obtaining the bulk Rashba and Dresselhaus terms (within the eight-band approach), and make the effective electron Hamiltonian energy independent (i.e., a *real* Schrödinger-type equation).

Through a self-consistent Schrödinger-Poisson calculation on GaN/AlGaN both single and double wells, involving either one or two occupied subbands, we have determined all the relevant SO strengths, i.e., the intrasubband Rashba α_ν ($\nu = 1, 2$) and Dresselhaus β_ν couplings, as well as the intersubband Rashba η and Dresselhaus Γ couplings. Our calculated spin-orbit coupling is in agreement with experimental data. We have also determined the several distinct constituents of the SO couplings due to the bulk, the Hartree, and the structural contributions, and find that the SO couplings follow from the interplay of all these terms. Particularly, we find that the bulk Rashba term dominates over all other remaining contributions to the intrasubband Rashba couplings. For our double wells, we find a *seemingly* symmetric configuration, at which both the intersubband Rashba and Dresselhaus couplings assume their largest values, due to a perfect overlap of the wave functions of the two subbands. On the other hand, across this configuration when we vary V_g , the intrasubband Dresselhaus couplings β_1 and β_2 almost interchange their values, a similar behavior also occurring for the Rashba couplings α_1 and α_2 . In addition, we have derived an effective spin-orbit Hamiltonian for electrons with arbitrary confining potentials and external magnetic fields, valid for quantum wells, wires, and dots.

As a final remark, although the SO couplings in our GaN wells are not sensitive (except for the double well around the seemingly symmetric configuration) to V_g , we emphasize that a sensitive electrical control of the Rashba couplings could be possible in narrow-gap wurtzite wells (e.g., GaAs with wurtzite structure), where the usual Rashba contributions (sensitive to V_g) could be comparable or even larger than the bulk contribution. Accordingly, since the Rashba and Dresselhaus SO fields have the same symmetry, it should be easy to attain both the weak and strong SO regimes, via a sensi-

tive electrical control of the Rashba couplings (both magnitude and sign). More interesting, it may be possible to tune $\alpha = -\beta$ in some parameter range, which would lead to a complete cancellation of the Rashba and Dresselhaus terms, thus rendering the spin a conserved quantity in wurtzite wells. This could possibly extend the SO-induced spin-flip times as compared to zincblende structures, provided that cubic contributions can be neglected. Additional work is needed to investigate this exciting possibility.

We hope that our general effective SO Hamiltonian stimulate further theoretical studies involving quantum wires and dots in wurtzite systems; these may be relevant, for instance, to wurtzite dot qubits.

ACKNOWLEDGMENTS

This work was supported by FAPESP grant No. 2016/08468-0, CNPq, PRP/USP (Q-NANO), the National Natural Science Foundation of China (Grant Nos. 11004120 and 11874236), and the Research Fund of Qufu Normal University. The authors acknowledge P. E. Faria Junior for useful discussions.

Appendix A: Effective Models via Group Theory and $k \cdot p$

As discussed in the main text, there are many different approaches in the literature to describe the band structure of a wurtzite crystal. Indeed, its bulk Hamiltonian has been written in many different basis sets [51], which might lead to inconsistencies among the models. In the main text, we have shown a comprehensive and detailed derivation of effective models for bulk wurtzite, as well as heterostructures (quantum wells, wires, and dots). In this appendix, we complement our discussion with a full and systematic derivation of the 2×2 electronic model and the 8×8 Kane Hamiltonian using group theory methods combined with the $k \cdot p$ approach. This provides a deeper understanding of the s - p_z mixing and justifies the choice of basis shown in Table I.

First, we present an alternative derivation of the effective electron Hamiltonian $\mathcal{H}(k_x, k_y)$ for the conduction band of wurtzite quantum wells near the Γ point. Next, we derive the 8×8 Kane model for bulk wurtzite. More specifically, we start with the CC basis [44], listed on the second column of Table III, and then discuss the transformation to the primed basis CC' , third column of Table III, which is the basis set we use throughout the main text (Sec. II B). As we will see below, the S' and Z' orbitals arise from the s - p_z mixing discussed in Ref. [35]. It is important to track the effects of this hybridization to establish all matrix elements allowed by symmetry and identify systematically the approximations used to obtain the final Kane model for wurtzite crystals.

The last column in Table III shows the irreducible representations (IRREPs) of the orbital part of the basis functions. Notice that, while zincblende crystals belong to the cubic T_d group, the wurtzite lattice belongs to the C_{6v}^4 . For T_d , the directions x , y , and z are all equivalent. However, on C_{6v} there

Table III. CC basis without $|\nu\rangle$ and with $|\nu'\rangle$ the s - p_z hybridization. Normalization requires $|q_s|^2 + |q_z|^2 = 1$. The q_s and q_z coefficients here match those of Ref. [35]. The orbitals S and Z belong to the IRREP Γ_1 (transform as scalars), while X and Y combine to form Γ_5 [transform as a (x, y) vector].

ν	$ \nu\rangle$	$ \nu'\rangle$	C_{6v} IRREP
1	$ iS \uparrow\rangle$	$ iS' \uparrow\rangle = q_s iS \uparrow\rangle + iq_z Z \uparrow\rangle$	Γ_1
2	$ iS \downarrow\rangle$	$ iS' \downarrow\rangle = q_s iS \downarrow\rangle + iq_z Z \downarrow\rangle$	Γ_1
3	$-\frac{1}{\sqrt{2}} X + iY \uparrow\rangle$	$-\frac{1}{\sqrt{2}} X + iY \uparrow\rangle$	Γ_5
4	$+\frac{1}{\sqrt{2}} X - iY \downarrow\rangle$	$+\frac{1}{\sqrt{2}} X - iY \downarrow\rangle$	Γ_5
5	$+\frac{1}{\sqrt{2}} X - iY \uparrow\rangle$	$+\frac{1}{\sqrt{2}} X - iY \uparrow\rangle$	Γ_5
6	$-\frac{1}{\sqrt{2}} X + iY \downarrow\rangle$	$-\frac{1}{\sqrt{2}} X + iY \downarrow\rangle$	Γ_5
7	$ Z \uparrow\rangle$	$ Z' \uparrow\rangle = q_s Z \uparrow\rangle + iq_z iS \uparrow\rangle$	Γ_1
8	$ Z \downarrow\rangle$	$ Z' \downarrow\rangle = q_s Z \downarrow\rangle + iq_z iS \downarrow\rangle$	Γ_1

is no symmetry constraint in the z direction, which makes the S and Z orbitals equivalent in terms of their symmetries (both belong to Γ_1). This reduced symmetry leads to the appearance of extra finite terms on wurtzite crystals. Nonetheless, this broken symmetry along the z axis can be considered “small” (quasi-cubic approximation [51]). Therefore, all new terms are expected to be small or negligible. Here, however, we present all these new terms allowed by symmetry and show their $\mathbf{k} \cdot \mathbf{p}$ expressions.

1. Theory of invariants

The theory of invariants [16, 35, 52] allows us to search for the most general form of the Hamiltonian $\mathcal{H}(\mathbf{k})$ allowed by the symmetries of the crystal. Namely, we can write

$$\mathcal{H}(\mathbf{k}) = \sum_{i,j,l} H_{i,j,l} k_x^i k_y^j k_z^l, \quad (\text{A1})$$

where $H_{i,j,l}$ are arbitrary matrices to be found. For 2D systems one can simply drop k_z and the sum over l .

The group of the Schrödinger equation is composed by the set of symmetry operations $\{O_i\}$ that keeps the crystal invariant. Consequently, these operations must commute with $\mathcal{H}(\mathbf{k})$, i.e., $[\mathcal{H}(\mathbf{k}), O_i] = 0$, yielding

$$\mathcal{H}(\mathbf{k}) = D_\psi(O_i) \mathcal{H}(D_k^{-1}(O_i)\mathbf{k}) D_\psi^{-1}(O_i), \quad (\text{A2})$$

in which $D_\psi(O_i)$ and $D_k(O_i)$ are the matrix representations of O_i in the Hilbert and k spaces, respectively. For each O_i , this imposes constraints on $\mathcal{H}(\mathbf{k})$, which can be then written as a system of coupled equations solved to find the allowed terms in each $H_{i,j,l}$.

The matrix representations of $D_\psi(O_i)$ and $D_k(O_i)$ can be found on the Bilbao Crystallographic Server [84–86]. These can be applied to the QSYMM [87] python package that solves the constraints imposed by Eq. (A2) and returns the most general expressions allowed by symmetry for $H_{i,j,l}$.

2. 2×2 electronic effective model

Let us now apply the theory of invariants to find the effective 2×2 model for our two-dimensional electron gas $\mathcal{H}(k_x, k_y)$ [for comparison, see upper left block of Eq. (40), i.e., the one-subband case].

Some materials, e.g., GaN and AlGaN, crystallize into the wurtzite structure, which belongs to the C_{6v}^4 (or $P6_3mc$) non-symmorphic space group [52]. At the Γ point, the first conduction bands are spin degenerate. Their orbital components transform as scalars (trivial representation), while the spinors transform as the $D_{1/2}$ double group IRREP, which is given by the generators of the $SU(2)$. These are equivalent to the $D_{1/2}$ IRREP of the symmorphic group C_{6v} . For simplicity, we use the point group notation for the operations $\{O_i\} = \{E, 2C_6, 2C_3, C_2, 3\sigma_d, 3\sigma_v\}$. In practice, it is sufficient to consider the generators $\{C_6, \sigma_d\}$, which correspond, respectively, to the six-fold rotations around the z axis and the $x \rightarrow -x$ mirror operations. Additionally, we also consider time-reversal symmetry \mathcal{T} . In the Hilbert space, these read

$$D_\psi(C_6) = \pm \exp\left(i\frac{\pi}{6}\sigma_z\right), \quad (\text{A3})$$

$$D_\psi(\sigma_d) = \pm \exp\left(i\frac{\pi}{2}\sigma_x\right), \quad (\text{A4})$$

$$D_\psi(\mathcal{T}) = i\sigma_y \mathcal{K}, \quad (\text{A5})$$

where \mathcal{K} is the complex conjugate, and the \pm signs refer to the 2π and 4π $SU(2)$ rotations. On the other hand, for the k -space representation, with $\mathbf{k} = (k_x \ k_y)^T$, we have

$$D_k(C_6) = \begin{bmatrix} \cos\left(\frac{2\pi}{6}\right) & \sin\left(\frac{2\pi}{6}\right) \\ -\sin\left(\frac{2\pi}{6}\right) & \cos\left(\frac{2\pi}{6}\right) \end{bmatrix}, \quad (\text{A6})$$

$$D_k(\sigma_d) = -\sigma_z, \quad (\text{A7})$$

$$D_k(\mathcal{T}) = -1_{2 \times 2}. \quad (\text{A8})$$

Substituting these representations into Eq. (A2), we find

$$H_{0,0} = h_0 1_{2 \times 2} \quad (\text{A9})$$

$$H_{1,0} = h_1 \sigma_y, \quad (\text{A10})$$

$$H_{0,1} = -h_1 \sigma_x, \quad (\text{A11})$$

$$H_{1,1} = 0_{2 \times 2}, \quad (\text{A12})$$

$$H_{2,0} = H_{0,2} = h_2 1_{2 \times 2} \quad (\text{A13})$$

with h_0 , h_1 , and h_2 arbitrary parameters. We can choose $h_0 = 0$, as it just results in an overall rigid shift. Moreover, we can identify $h_1 = \alpha$ and $h_2 = \hbar^2/2m^*$, yielding

$$\mathcal{H}(k_x, k_y) = \alpha(k_x \sigma_y - k_y \sigma_x) + \frac{\hbar^2}{2m^*}(k_x^2 + k_y^2). \quad (\text{A14})$$

The effective mass m^* and the spin-orbit coupling α here remain as unknown parameters. These can be obtained by fitting *ab initio* or experimental data. A more insightful approach, however, is to start from the 8×8 Kane model – derived in the next section – and project its solutions onto the electron subspace as developed in the main text.

3. 8×8 Kane model: method of invariants

We apply the method of invariants to obtain the most general 8×8 Kane model considering the basis states shown in Table III. Differently from the previous section, here we follow a single group formulation, which matches the CC basis, and maintain the spins along z as good quantum numbers for the basis set. The representations for the generators $\{C_6, \sigma_d\}$ and the time-reversal operator \mathcal{T} follow from the IRREPs Γ_1 and Γ_5 of the C_{6v} point group. Applying the constraints of the theory of invariants, we obtain the following 8×8 model in the CC basis $|\nu\rangle$

$$\begin{aligned}
 H_{8 \times 8} = & \begin{pmatrix} c_0 & 0 & 0 & 0 & 0 & ic_5 & ic_6 & 0 \\ 0 & c_0 & 0 & 0 & ic_5 & 0 & 0 & ic_6 \\ 0 & 0 & c_1 & 0 & 0 & 0 & 0 & 0 \\ 0 & 0 & 0 & c_1 & 0 & 0 & 0 & 0 \\ 0 & -ic_5 & 0 & 0 & c_2 & 0 & 0 & c_3 \\ -ic_5 & 0 & 0 & 0 & 0 & c_2 & c_3 & 0 \\ -ic_6 & 0 & 0 & 0 & 0 & c_3 & c_4 & 0 \\ 0 & -ic_6 & 0 & 0 & c_3 & 0 & 0 & c_4 \end{pmatrix} \\
 & + \begin{pmatrix} 0 & ic_7^- & c_{13}^+ & 0 & -c_{14}^- & 0 & 0 & -c_{15}^- \\ -ic_7^+ & 0 & 0 & -c_{13}^- & 0 & c_{14}^+ & c_{15}^+ & 0 \\ c_{13}^- & 0 & 0 & 0 & 0 & ic_8^- & ic_9^- & 0 \\ 0 & -c_{13}^+ & 0 & 0 & -ic_8^+ & 0 & 0 & ic_9^+ \\ -c_{14}^- & 0 & 0 & +ic_8^+ & 0 & -ic_{10}^- & -ic_{11}^- & 0 \\ 0 & c_{14}^+ & -ic_8^- & 0 & +ic_{10}^+ & 0 & 0 & ic_{11}^+ \\ 0 & c_{15}^- & -ic_9^+ & 0 & +ic_{11}^- & 0 & 0 & ic_{12}^- \\ -c_{15}^+ & 0 & 0 & -ic_9^- & 0 & -ic_{11}^+ & -ic_{12}^+ & 0 \end{pmatrix} k_{\pm} \\
 & + \begin{pmatrix} 0 & 0 & 0 & 0 & 0 & c_{16} & c_{17} & 0 \\ 0 & 0 & 0 & 0 & c_{16} & 0 & 0 & c_{17} \\ 0 & 0 & 0 & 0 & 0 & 0 & 0 & 0 \\ 0 & 0 & 0 & 0 & 0 & 0 & 0 & 0 \\ 0 & c_{16} & 0 & 0 & 0 & 0 & 0 & ic_{18} \\ c_{16} & 0 & 0 & 0 & 0 & 0 & ic_{18} & 0 \\ c_{17} & 0 & 0 & 0 & 0 & -ic_{18} & 0 & 0 \\ 0 & c_{17} & 0 & 0 & -ic_{18} & 0 & 0 & 0 \end{pmatrix} k_z, \quad (\text{A15})
 \end{aligned}$$

where c_n , $n = 0, \dots, 18$, are unknown coefficients allowed by symmetry, which later on will be defined in terms of the $\mathbf{k} \cdot \mathbf{p}$ parameters. The first matrix above corresponds to the k -independent terms, the second matrix gives the terms c_n^{\pm} linear in $k_{\pm} = k_x \pm ik_y$, and the third matrix represents the k_z -linear terms. For simplicity, we do not show the k_x^2 , k_y^2 , and k_z^2 terms.

The model in Eq. (A15) is built solely based on the symmetries of the basis set. However, the IRREPs that define the $|\nu\rangle$ and $|\nu'\rangle$ basis sets are the same, as shown in Table III. Hence, up to this point, the model above does not distinguish between different basis sets with equivalent symmetries. To proceed we must specify the basis and identify the matrix elements c_n in terms of the $\mathbf{k} \cdot \mathbf{p}$ theory.

4. 8×8 Kane model: $\mathbf{k} \cdot \mathbf{p}$ approach

Here we consider $H = H_0^{\text{CC}} + W^{\text{CC}}(\mathbf{k})$, with

$$H_0^{\text{CC}} = \frac{p^2}{2m_0} + V(\mathbf{r}) + H_{\text{so}z}, \quad (\text{A16})$$

$$W^{\text{CC}}(\mathbf{k}) = \frac{\hbar}{m_0} \mathbf{k} \cdot \boldsymbol{\pi} + H_{\text{so}x} + H_{\text{so}y}, \quad (\text{A17})$$

$$H_{\text{so}j} = C \left(\nabla V(\mathbf{r}) \times \mathbf{p} \right)_j \sigma_j, \quad (\text{A18})$$

$$\boldsymbol{\pi} = \mathbf{p} + C \left[\boldsymbol{\sigma} \times \nabla V(\mathbf{r}) \right], \quad (\text{A19})$$

where $C = \hbar/4m_0^2c^2$ defines the SO coupling intensity.

Below we first show how a commutator trick [35] can be used to simplify some matrix elements and later we identify the matrix elements using the $\mathbf{k} \cdot \mathbf{p}$ model above.

a. Selection rules and commutator trick

As shown in Eq. (A16), we choose to keep only the z -component of H_{so} in H_0^{CC} , such that the spin remains a good quantum number. In addition, this choice allows us to use a commutator trick introduced in Ref. [35] to eliminate a few matrix elements. Namely, the matrix elements of $C\sigma_x V_z \equiv C\sigma_x \partial_z V$, which can be written as

$$C \langle \nu_1 \uparrow | \sigma_x V_z | \nu_2 \downarrow \rangle = C \langle \nu_1 \uparrow | V_z | \nu_2 \uparrow \rangle, \quad (\text{A20})$$

$$\begin{aligned}
 C \langle \nu_1 \uparrow | \sigma_x V_z | \nu_2 \downarrow \rangle &= -\frac{i}{\hbar} C \langle \nu_1 \uparrow | [V, p_z] | \nu_2 \uparrow \rangle \\
 &= -\frac{i}{\hbar} C \langle \nu_1 \uparrow | [H_0^{\text{CC}} - H_{\text{so}z}, p_z] | \nu_2 \uparrow \rangle \\
 &= -\frac{i}{\hbar} C \left[(\varepsilon_{\nu_1 \uparrow} - \varepsilon_{\nu_2 \uparrow}) \langle \nu_1 \uparrow | p_z | \nu_2 \uparrow \rangle \right. \\
 &\quad \left. - \langle \nu_1 \uparrow | [H_{\text{so}z}, p_z] | \nu_2 \uparrow \rangle \right] \\
 &= \frac{i}{\hbar} C \langle \nu_1 \uparrow | [H_{\text{so}z}, p_z] | \nu_2 \uparrow \rangle. \quad (\text{A21})
 \end{aligned}$$

Here $|\nu\sigma\rangle$ are the eigenstates of H_0^{CC} with eigenenergies $\varepsilon_{\nu\sigma}$. Similar expressions hold for the matrix elements of $C\sigma_y V_z$. In Eq. (A20), we have simply acted σ_x on the ket, while in Eq. (A21), we have used the identity $\partial_z V \equiv -i[V, p_z]/\hbar \equiv -i[H_0^{\text{CC}} - H_{\text{so}z}, p_z]$. The last line in (A21) is only valid if the eigenstates are degenerate, i.e., $\varepsilon_{\nu_1 \uparrow} = \varepsilon_{\nu_2 \uparrow}$. Below we show that this type of matrix element, either in the form (A20) or (A21), is identically zero or negligible.

Let us first consider the matrix element in the form (A20). The operator V_z transforms as Γ_1 , while the eigenstates transform either as Γ_1 or Γ_5 (see Table III). Therefore, the selection rules already dictate that the matrix element is zero if $|\nu_1 \sigma_1\rangle$ and $|\nu_2 \sigma_2\rangle$ belong to different IRREPs.

On the other hand, if they belong to the same IRREP $\Gamma_{\nu_1} = \Gamma_{\nu_2} = \Gamma_j$ ($j = 1$ or 5), we have to argue differently, since

$\Gamma_1 \otimes \Gamma_1 = \Gamma_1$, and $\Gamma_5 \otimes \Gamma_5 \supset \Gamma_1$. Consider then the form (A21) for degenerate states ($\varepsilon_{v_1\uparrow} = \varepsilon_{v_2\uparrow}$). Notice that the operator $[H_{\text{soz}}, p_z]$ transforms as Γ_2 . The matrix element transforms as $\Gamma_j \otimes \Gamma_2 \otimes \Gamma_j$ and two cases are possible:

- (a) $\Gamma_{v_1} = \Gamma_{v_2} = \Gamma_1$: $\Gamma_1 \otimes \Gamma_2 \otimes \Gamma_1 = \Gamma_2$, which yields $\langle v_1 \uparrow | [H_{\text{soz}}, p_z] | v_2 \downarrow \rangle = 0$;
- (b) $\Gamma_{v_1} = \Gamma_{v_2} = \Gamma_5$: $\Gamma_5 \otimes \Gamma_2 \otimes \Gamma_5 \supset \Gamma_1$, which allows for $\langle v_1 \uparrow | [H_{\text{soz}}, p_z] | v_2 \downarrow \rangle \neq 0$.

It is easy to see, though, that the nonzero matrix element in (b) results in a negligible higher order correction, since $\frac{i}{\hbar} C \langle v_1 \uparrow | [H_{\text{soz}}, p_z] | v_2 \downarrow \rangle \propto C^2$. We shall point out that this leads to the term α_2 obtained in Ref [41].

In summary, the matrix elements of $\langle v_1 \uparrow | \sigma_\mu V_z | v_2 \downarrow \rangle$, with $\mu = \{x, y\}$, are

- (1) identically zero
 - (i) if $|v_1 \uparrow\rangle$ and $|v_2 \downarrow\rangle$ belong to different IRREPs;
 - (ii) if $\varepsilon_{v_1\uparrow} = \varepsilon_{v_2\uparrow}$ and $|v_1 \uparrow\rangle$ and $|v_2 \downarrow\rangle$ belong to the Γ_1 IRREP.
- (2) negligible ($\propto C^2$)
 - (i) if $\varepsilon_{v_1\uparrow} = \varepsilon_{v_2\uparrow}$ and $|v_1 \uparrow\rangle$ and $|v_2 \downarrow\rangle$ belong to the Γ_5 IRREP.

Notice that, due to the spin-flip induced by the σ_μ operator acting on the matrix element, the states $|v_1 \uparrow\rangle$ and $|v_2 \uparrow\rangle$ must have the same energies, instead of $|v_1 \uparrow\rangle$ and $|v_2 \downarrow\rangle$.

The selection rules above rely on the form of our Hamiltonian given in Eqs. (A16) and (A17). This is a partially relativistic model, accounting only for the SO correction. Additionally, one could consider the scalar relativistic corrections, namely the mass-velocity $H_{mv} = \frac{p^4}{8m_0^3c^2}$ and the Darwin $H_D = \frac{\hbar^2}{8m_0^2c^2} \nabla^2 V(\mathbf{r})$ terms. Both transform as Γ_1 and might contribute to the $k = 0$ diagonal matrix elements (band edges) and to the s - p_z hybridization [c_6 term in Eq. (A15)]. More importantly, these would also appear added to H_{soz} in Eq. (A21), possibly affecting the selection rule (1-ii). The mass-velocity term vanishes as $[H_{mv}, p_z] = 0$. However, the Darwin term breaks the selection rule $[H_D, p_z] \neq 0$. Nonetheless, since the latter arises from the fine structure, it scales with $H_D \propto C$, yielding again a negligible contribution $C \langle v_1 \uparrow | \sigma_x V_z | v_2 \downarrow \rangle = \frac{i}{\hbar} C \langle v_1 \uparrow | [H_D, p_z] | v_2 \uparrow \rangle \propto C^2$. This correction allows for the γ_1 and α_3 terms in Ref. [41].

b. Matrix elements

Next, let us follow the $\mathbf{k} \cdot \mathbf{p}$ approach and identify the leading order contributions for each $\mathbf{k} = 0$ term in $H_{8 \times 8}$ from

Eq. (A15). After simplifications, these are

$$\begin{aligned} c_0 &= \langle iS \uparrow | \frac{p^2}{2m_0} + V(\mathbf{r}) | iS \uparrow \rangle, \\ c_4 &= \langle Z \uparrow | \frac{p^2}{2m_0} + V(\mathbf{r}) | Z \uparrow \rangle, \\ ic_6 &= \langle iS \uparrow | \frac{p^2}{2m_0} + V(\mathbf{r}) | Z \uparrow \rangle, \\ c_3 &= +\sqrt{2}C \langle X - iY \uparrow | V_y p_z - V_z p_y | Z \uparrow \rangle, \\ -ic_5 &= +\sqrt{2}C \langle X - iY \uparrow | V_y p_x - V_z p_y | iS \uparrow \rangle. \end{aligned}$$

Both c_6 and c_5 are nonzero due to the broken wurtzite symmetry along z (in zincblende $c_6 = c_5 = 0$). It remains to define $c_1 = c_X + \delta c_X$ and $c_2 = c_X - \delta c_X$, in which

$$\begin{aligned} c_X &= \frac{1}{2} \langle X + iY \uparrow | \frac{p^2}{2m_0} + V(\mathbf{r}) | X + iY \uparrow \rangle, \\ \delta c_X &= \frac{1}{2} C \langle X + iY \uparrow | V_x p_y - V_y p_x | X + iY \uparrow \rangle. \end{aligned}$$

To properly use the commutator trick introduced in Eq. (A21), it is important to keep track of the matrix form of H_0^{CC} , which includes only the z -component of the SO coupling. Within this non-primed basis, we get

$$H_0^{\text{CC}} = \begin{pmatrix} c_0 & 0 & 0 & 0 & 0 & 0 & ic_6 & 0 \\ 0 & c_0 & 0 & 0 & 0 & 0 & 0 & ic_6 \\ 0 & 0 & c_1 & 0 & 0 & 0 & 0 & 0 \\ 0 & 0 & 0 & c_1 & 0 & 0 & 0 & 0 \\ 0 & 0 & 0 & 0 & c_2 & 0 & 0 & 0 \\ 0 & 0 & 0 & 0 & 0 & c_2 & 0 & 0 \\ -ic_6 & 0 & 0 & 0 & 0 & 0 & c_4 & 0 \\ 0 & -ic_6 & 0 & 0 & 0 & 0 & 0 & c_4 \end{pmatrix}.$$

The term c_6 is the one responsible for the s - p_z mixing [35], as it couples the states $|S\rangle$ and $|Z\rangle$.

The finite terms on the k_z block of $H_{8 \times 8}$ are

$$\begin{aligned} c_{16} &= \frac{\hbar}{m_0} \frac{C}{\sqrt{2}} \langle X - iY \uparrow | V_y + iV_x | iS \uparrow \rangle, \\ ic_{18} &= \frac{\hbar}{m_0} \frac{C}{\sqrt{2}} \langle X - iY \uparrow | V_y + iV_x | Z \uparrow \rangle, \\ c_{17} &= \frac{\hbar}{m_0} \langle iS \uparrow | p_z | Z \uparrow \rangle = P_1. \end{aligned}$$

The term c_{16} is allowed in both zincblende and wurtzite, while c_{18} only in wurtzite. However, one typically neglects these k -dependent SO terms. The term c_{17} gives us the Kane parameter P_1 , also present in the CC original paper [44].

The k_{\pm} -dependent terms of $H_{8 \times 8}$ are given by

$$\begin{aligned}
ic_8 &= \frac{\hbar}{m_0} \frac{C}{2} \langle X + iY \uparrow | \sigma_y V_z | X + iY \downarrow \rangle, \\
ic_7 &= -i \frac{\hbar C}{m_0} \langle iS \uparrow | V_z | iS \uparrow \rangle, \\
ic_{10} &= -i \frac{\hbar C}{2m_0} \langle X - iY \uparrow | V_z | X + iY \uparrow \rangle, \\
ic_{12} &= -i \frac{\hbar C}{m_0} \langle Z \uparrow | V_z | Z \uparrow \rangle, \\
c_{15} &= -i \frac{\hbar C}{m_0} \langle Z \uparrow | V_z | iS \uparrow \rangle, \\
ic_9 &= \frac{\hbar}{\sqrt{2}m_0} \left[\langle X - iY \downarrow | p_x | Z \downarrow \rangle + C \langle X - iY \downarrow | V_y | Z \downarrow \rangle \right], \\
ic_{11} &= \frac{-\hbar}{\sqrt{2}m_0} \left[\langle X + iY \downarrow | p_x | Z \downarrow \rangle + C \langle X + iY \downarrow | V_y | Z \downarrow \rangle \right], \\
c_{13} &= \frac{-\hbar}{\sqrt{2}m_0} \left[\langle X - iY \downarrow | p_x | iS \downarrow \rangle + C \langle X - iY \downarrow | V_y | iS \downarrow \rangle \right], \\
c_{14} &= \frac{-\hbar}{\sqrt{2}m_0} \left[\langle X + iY \downarrow | p_x | iS \downarrow \rangle + C \langle X + iY \downarrow | V_y | iS \downarrow \rangle \right].
\end{aligned} \tag{A22}$$

The k -dependent SO components in c_{13} and c_{14} are usually neglected, which leads to $c_{13} = c_{14}$ for both zinc-blend and wurtzite. Under the same approximation, c_7 , c_{10} , c_{12} , and c_{15} can be neglected. Terms $c_9 \approx -c_{11}$ can be neglected under the quasi-cubic assumption. As mentioned above, we cannot use the commutator trick to eliminate c_7 and c_{12} , since $|iS \uparrow\rangle$ and $|Z \uparrow\rangle$ are not eigenstates of H_0^{CC} due to the possible s - p_z mixing introduced by c_6 . This is a strong motivation to change to the primed basis $|\nu'\rangle$ from Table III, which will not only eliminate c_6 through a rotation, but will also allow us to use the selection rules and the commutator trick to simplify the final model.

c. Changing basis: s - p_z mixing

To eliminate the term c_6 , the $|\nu'\rangle$ basis is defined by the coefficients q_s and q_z given by the eigenstates of the submatrix $\begin{pmatrix} c_0 & ic_6 \\ -ic_6 & c_4 \end{pmatrix}$, which read

$$q_s \approx 1 - \frac{1}{2} \left(\frac{c_6}{c_0 - c_4} \right)^2, \quad q_z \approx - \left(\frac{c_6}{c_0 - c_4} \right). \tag{A23}$$

As expected, q_s is defined by the ratio between the coupling c_6 and the gap $c_0 - c_4 = \varepsilon_{1\uparrow} - \varepsilon_{8\uparrow}$, hence $|q_z| \ll |q_s|$. The resulting primed basis $|\nu'\rangle$ diagonalizes H_0^{CC} ,

$$H_0^{\text{CC}} = \begin{pmatrix} c'_0 & 0 & 0 & 0 & 0 & 0 & 0 & 0 \\ 0 & c'_0 & 0 & 0 & 0 & 0 & 0 & 0 \\ 0 & 0 & c_1 & 0 & 0 & 0 & 0 & 0 \\ 0 & 0 & 0 & c_1 & 0 & 0 & 0 & 0 \\ 0 & 0 & 0 & 0 & c_2 & 0 & 0 & 0 \\ 0 & 0 & 0 & 0 & 0 & c_2 & 0 & 0 \\ 0 & 0 & 0 & 0 & 0 & 0 & c'_4 & 0 \\ 0 & 0 & 0 & 0 & 0 & 0 & 0 & c'_4 \end{pmatrix}.$$

Let us now show the general Hamiltonian $H'_{8 \times 8}$ within the $|\nu'\rangle$ basis, with all symmetry allowed terms. In the next section we will select only the relevant matrix elements to build our final model. As previously done, we break the new Hamiltonian as $H'_{8 \times 8} = H'_0 + H'_z k_z + H'_{\pm} k_{\pm}$.

The Hamiltonian H'_0 reads

$$H'_0 = H_0^{\text{CC}} + \begin{pmatrix} 0 & 0 & 0 & 0 & 0 & ic'_5 & 0 & 0 \\ 0 & 0 & 0 & 0 & ic'_5 & 0 & 0 & 0 \\ 0 & 0 & +\delta c_X & 0 & 0 & 0 & 0 & 0 \\ 0 & 0 & 0 & +\delta c_X & 0 & 0 & 0 & 0 \\ 0 & -ic'_5 & 0 & 0 & -\delta c_X & 0 & 0 & c'_3 \\ -ic'_5 & 0 & 0 & 0 & 0 & -\delta c_X & c'_3 & 0 \\ 0 & 0 & 0 & 0 & 0 & c'_3 & 0 & 0 \\ 0 & 0 & 0 & 0 & c'_3 & 0 & 0 & 0 \end{pmatrix},$$

with

$$\begin{aligned}
c'_0 &= q_s^2 c_0 + q_z^2 c_4 - 2q_s q_z c_6 = \langle iS' \uparrow | \frac{p^2}{2m_0} + V(\mathbf{r}) | iS' \uparrow \rangle, \\
c'_4 &= q_s^2 c_4 + q_z^2 c_0 + 2q_s q_z c_6 = \langle Z' \uparrow | \frac{p^2}{2m_0} + V(\mathbf{r}) | Z' \uparrow \rangle, \\
c'_3 &= q_s c_3 + q_z c_5 = +\sqrt{2}C \langle X - iY \uparrow | V_y p_z - V_z p_y | Z' \uparrow \rangle, \\
c'_5 &= q_s c_5 - q_z c_3 = i\sqrt{2}C \langle X - iY \uparrow | V_y p_z - V_z p_y | iS' \uparrow \rangle.
\end{aligned}$$

All c'_j matrix elements are similar to their non-primed c_j counterparts, except for the the replacements $S \rightarrow S'$ and $Z \rightarrow Z'$. The same is valid for the finite k_z and k_{\pm} terms below. Indeed, for the k_z -linear terms, H'_z keeps the same form as its non-primed counterpart in $H_{8 \times 8}$, with the coefficients replaced by its primed versions as

$$\begin{aligned}
c'_{17} &= c_{17} = \frac{\hbar}{m_0} \langle iS' \uparrow | p_z | Z' \uparrow \rangle, \\
c'_{16} &= q_s c_{16} - q_z c_{18} = \frac{\hbar}{m_0} \frac{C}{\sqrt{2}} \langle X - iY \uparrow | V_y + iV_x | iS' \uparrow \rangle, \\
c'_{18} &= q_s c_{18} + q_z c_{16} = -i \frac{\hbar}{m_0} \frac{C}{\sqrt{2}} \langle X - iY \uparrow | V_y + iV_x | Z' \uparrow \rangle.
\end{aligned}$$

As mentioned above, c'_{16} and c'_{18} are k -dependent SO terms that are usually neglected, while $c'_{17} = P_1$ is one of the usual Kane parameters.

The change of basis truly pays off due to the simplifications on H'_{\pm} . We can now use the commutator trick to further eliminate

$$ic'_7 = -i \frac{\hbar C}{m_0} \langle iS' \uparrow | V_z | iS' \uparrow \rangle = 0,$$

$$ic'_{12} = -i \frac{\hbar C}{m_0} \langle Z' \uparrow | V_z | Z' \uparrow \rangle = 0.$$

Therefore, we get

$$H'_{\pm} = \begin{pmatrix} 0 & 0 & c'_{13} & 0 & -c'_{14} & 0 & 0 & -c'_{15} \\ 0 & 0 & 0 & -c'_{13} & 0 & c'_{14} & c'_{15} & 0 \\ c'_{13} & 0 & 0 & 0 & 0 & 0 & ic'_9 & 0 \\ 0 & -c'_{13} & 0 & 0 & 0 & 0 & 0 & ic'_9 \\ -c'_{14} & 0 & 0 & 0 & 0 & -ic'_{10} & -ic'_{11} & 0 \\ 0 & c'_{14} & 0 & 0 & +ic'_{10} & 0 & 0 & ic'_{11} \\ 0 & c'_{15} & -ic'_9 & 0 & +ic'_{11} & 0 & 0 & 0 \\ -c'_{15} & 0 & 0 & -ic'_9 & 0 & -ic'_{11} & 0 & 0 \end{pmatrix},$$

with $c'_{10} = c_{10}$, and

$$\begin{aligned} ic'_9 &= \frac{\hbar}{\sqrt{2}m_0} \left[\langle X - iY \downarrow | p_x | Z' \downarrow \rangle + C \langle X - iY \downarrow | V_y | Z' \downarrow \rangle \right], \\ ic'_{11} &= \frac{-\hbar}{\sqrt{2}m_0} \left[\langle X + iY \downarrow | p_x | Z' \downarrow \rangle + C \langle X + iY \downarrow | V_y | Z' \downarrow \rangle \right], \\ c'_{13} &= \frac{-\hbar}{\sqrt{2}m_0} \left[\langle X - iY \downarrow | p_x | iS' \downarrow \rangle + C \langle X - iY \downarrow | V_y | iS' \downarrow \rangle \right], \\ c'_{14} &= \frac{-\hbar}{\sqrt{2}m_0} \left[\langle X + iY \downarrow | p_x | iS' \downarrow \rangle + C \langle X + iY \downarrow | V_y | iS' \downarrow \rangle \right], \\ c'_{15} &= -i \frac{\hbar C}{m_0} \langle Z' \uparrow | V_z | iS' \uparrow \rangle. \end{aligned}$$

d. Approximations and final model

Up to this point, the results above are exactly derived from the symmetry constraints and selection rules from §4.4a. In the following, we introduce the approximations that lead to the final model $H_{8 \times 8}^{\text{CC}}$ shown in Eq. (7) of the main text.

If one is interested in the electron bands, it is usual to neglect the k -dependent SO terms, which only contribute in high orders to the Lwdin partitioning. This approximation eliminates $c'_{10} \approx c'_{15} \approx c'_{16} \approx c'_{18} \approx 0$. Moreover, it allows us to neglect the SO contribution in $c'_9, c'_{11}, c'_{13}, c'_{14}$, which yields $c'_{13} \approx c'_{14} \equiv -P_2/\sqrt{2}$ as a Kane parameter, while $c'_9 \approx -c'_{11} \approx 0$ within the quasi-cubic approximation. We have already defined $c'_{17} = P_1$. For the $\mathbf{k} = 0$ terms, it follows that $c'_0 = E_c, c_X = E_v + \Delta_1, \delta c_X = \Delta_2, c'_4 = E_v, c'_3 = \sqrt{2}\Delta_3$, and $c'_5 = -\sqrt{2}\Delta_{sz}$. By setting $E_c = 0$ (energy reference) and $E_v + \Delta_1 + \Delta_2 = -E_g$, we have $c'_0 = 0, c'_1 = -E_g, c'_2 = -E_g - 2\Delta_2$, and $c'_4 = -E_g - \Delta_1 - \Delta_2$. Under these assumptions, the $H_{8 \times 8}^{\text{CC}}$ from the previous section yields our model $H_{8 \times 8}^{\text{CC}}$ shown in Eq. (7).

e. Remarks on Δ_3 and Δ_{sz}

For most of the terms above, the difference between the primed c'_j and non-primed c_j matrix elements is nearly irrelevant. However, it is worth noting that this is not the case for the terms c'_3 and c'_5 .

We have shown that $c'_3 = q_s c_3 + q_z c_5$. Let us assume that the s - p_z hybridization is small, it follows that $q_z \ll q_s$ and we can take $q_s \approx 1$. The dominant contribution is $c'_3 \approx c_3$, which gives us

$$\begin{aligned} \Delta_3 &= \frac{c'_3}{\sqrt{2}} = C \langle X - iY \uparrow | V_y p_z - V_z p_y | Z' \uparrow \rangle, \\ &\approx \frac{c_3}{\sqrt{2}} = C \langle X - iY \uparrow | V_y p_z - V_z p_y | Z \uparrow \rangle. \end{aligned} \quad (\text{A24})$$

The case for the term $c'_5 = -\sqrt{2}\Delta_{sz}$ is more delicate. The s - p_z hybridization leads to $c'_5 = q_s c_5 - q_z c_3$, which may be

written as

$$\begin{aligned} \Delta_{sz} &= -\frac{q_s c_5 - q_z c_3}{\sqrt{2}} = -q_s \frac{c_5}{\sqrt{2}} + q_z \Delta_3 = \\ &= C \left[-iq_s \langle X - iY \uparrow | V_y p_z - V_z p_y | iS \uparrow \rangle \right. \\ &\quad \left. + q_z \langle X - iY \uparrow | V_y p_z - V_z p_y | Z \uparrow \rangle \right]. \end{aligned}$$

Notice that both matrix elements above arise from the k -independent SO term and are nearly identical, except for the change $|iS \uparrow\rangle \leftrightarrow |Z \uparrow\rangle$. Therefore, we may wonder which contribution prevails. One can argue that the first matrix element (arising from c_5 , with $|iS \uparrow\rangle$) is small under the quasi-cubic approximation. However, it multiplies $q_s \approx 1$. On the other hand, the second term (arising from Δ_3 , with $|Z \uparrow\rangle$) is finite even in zincblende, but multiplies $|q_z| \ll |q_s|$. Thus, it is not possible to define the dominant term *a priori*.

Typically, one argues in favor of the quasi-cubic approximation to parametrize $\Delta_{sz} \approx q_z \Delta_3$ in terms of Δ_3 , using q_z as a free fitting parameter. However, the analysis above shows that this is not a good and systematic approach. Instead, we consider that it is better to keep Δ_{sz} itself as an independent parameter for wurtzite crystals. Notice that Δ_{sz} naturally vanishes in zincblende, for which $c_5 = q_z = 0$.

Appendix B: Kane model – diagonal basis

Here we obtain the real band edges and the corresponding basis set $u_{i0}(\mathbf{r})$ that diagonalizes the Hamiltonian $H_0^{\text{diag}} = H_0^{\text{CC}} + H_{\text{sox}} + H_{\text{soy}}$ at $\mathbf{k} = 0$.

1. Unstrained case

The actual band edges and corresponding basis functions $u_{i0}(\mathbf{r})$ without strain can be obtained by diagonalizing the corresponding CC-basis Kane model [Eqs. (7)] at $\mathbf{k} = 0$. The energy differences between the band edges, shown in Fig. 1(a) (neglecting Δ_{sz}), are given by

$$E_{AB} = \frac{1}{2}(\Delta_{\text{cr}} + 3\Delta_2) - \frac{1}{2}\sqrt{(\Delta_{\text{cr}} - \Delta_2)^2 + 8\Delta_3^2}, \quad (\text{B1})$$

$$E_{AC} = \frac{1}{2}(\Delta_{\text{cr}} + 3\Delta_2) + \frac{1}{2}\sqrt{(\Delta_{\text{cr}} - \Delta_2)^2 + 8\Delta_3^2}, \quad (\text{B2})$$

$$E_{BC} = E_{AC} - E_{AB} = \sqrt{(\Delta_{\text{cr}} - \Delta_2)^2 + 8\Delta_3^2}. \quad (\text{B3})$$

The diagonal basis $u_{i0}(\mathbf{r})$ shown in Table IV has the following normalization constants

$$A_i = 1/\sqrt{1 + \frac{2c_1^2 \Delta_{sz}^2}{(E_g + E_{AB} + E_i)^2} + \frac{2c_2^2 \Delta_{sz}^2}{(E_g + E_{AC} + E_i)^2}}, \quad (\text{B4})$$

Table IV. Real band edges λ_i (E_i) with $i = e, A, B, C$ and corresponding eigenfunctions $u_i \equiv u_{i0}(\mathbf{r})$ of H_0 at $\mathbf{k} = 0$. The relevant constants A_i , c_1 , c_2 , E_{AB} , and E_{AC} are defined in Eqs. (B3)–(B4). The eigenenergy λ_i (E_i) corresponds to the band edge energy with (without) the s - p_z mixing contribution. The difference between λ_i and E_i is less than 10^{-3} meV.

E_i	u_i
$\lambda_e \simeq E_e$	$ u_1\rangle = A_{\lambda_e} \left[iS' \uparrow\rangle - \left(\frac{c_1^2}{E_g + E_{AB} + \lambda_e} + \frac{c_2^2}{E_g + E_{AC} + \lambda_e} \right) i\Delta_{sz} (X \downarrow\rangle + i Y \downarrow\rangle) + i\sqrt{2}c_1c_2\Delta_{sz} \left(\frac{1}{E_g + E_{AB} + \lambda_e} - \frac{1}{E_g + E_{AC} + \lambda_e} \right) Z' \uparrow\rangle \right]$
$\lambda_e \simeq E_e$	$ u_2\rangle = A_{\lambda_e} \left[iS' \downarrow\rangle + \left(\frac{c_1^2}{E_g + E_{AB} + \lambda_e} + \frac{c_2^2}{E_g + E_{AC} + \lambda_e} \right) i\Delta_{sz} (X \uparrow\rangle - i Y \uparrow\rangle) + i\sqrt{2}c_1c_2\Delta_{sz} \left(\frac{1}{E_g + E_{AB} + \lambda_e} - \frac{1}{E_g + E_{AC} + \lambda_e} \right) Z' \downarrow\rangle \right]$
$\lambda_A \simeq E_A$	$ u_3\rangle = -\frac{1}{\sqrt{2}} (X \uparrow\rangle + i Y \uparrow\rangle)$
$\lambda_A \simeq E_A$	$ u_4\rangle = \frac{1}{\sqrt{2}} (X \downarrow\rangle - i Y \downarrow\rangle)$
$\lambda_B \simeq E_B$	$ u_5\rangle = A_{\lambda_B} \left[iS' \uparrow\rangle - \left(\frac{c_1^2}{E_g + E_{AB} + \lambda_B} + \frac{c_2^2}{E_g + E_{AC} + \lambda_B} \right) i\Delta_{sz} (X \downarrow\rangle + i Y \downarrow\rangle) + i\sqrt{2}c_1c_2\Delta_{sz} \left(\frac{1}{E_g + E_{AB} + \lambda_B} - \frac{1}{E_g + E_{AC} + \lambda_B} \right) Z' \uparrow\rangle \right]$
$\lambda_B \simeq E_B$	$ u_6\rangle = A_{\lambda_B} \left[iS' \downarrow\rangle + \left(\frac{c_1^2}{E_g + E_{AB} + \lambda_B} + \frac{c_2^2}{E_g + E_{AC} + \lambda_B} \right) i\Delta_{sz} (X \uparrow\rangle - i Y \uparrow\rangle) + i\sqrt{2}c_1c_2\Delta_{sz} \left(\frac{1}{E_g + E_{AB} + \lambda_B} - \frac{1}{E_g + E_{AC} + \lambda_B} \right) Z' \downarrow\rangle \right]$
$\lambda_C \simeq E_C$	$ u_7\rangle = A_{\lambda_C} \left[iS' \uparrow\rangle - \left(\frac{c_1^2}{E_g + E_{AB} + \lambda_C} + \frac{c_2^2}{E_g + E_{AC} + \lambda_C} \right) i\Delta_{sz} (X \downarrow\rangle + i Y \downarrow\rangle) + i\sqrt{2}c_1c_2\Delta_{sz} \left(\frac{1}{E_g + E_{AB} + \lambda_C} - \frac{1}{E_g + E_{AC} + \lambda_C} \right) Z' \uparrow\rangle \right]$
$\lambda_C \simeq E_C$	$ u_8\rangle = A_{\lambda_C} \left[iS' \downarrow\rangle + \left(\frac{c_1^2}{E_g + E_{AB} + \lambda_C} + \frac{c_2^2}{E_g + E_{AC} + \lambda_C} \right) i\Delta_{sz} (X \uparrow\rangle - i Y \uparrow\rangle) + i\sqrt{2}c_1c_2\Delta_{sz} \left(\frac{1}{E_g + E_{AB} + \lambda_C} - \frac{1}{E_g + E_{AC} + \lambda_C} \right) Z' \downarrow\rangle \right]$

where A_i ($i=e, A, B,$ and C) and

$$c_1 = \frac{E_{AC} - 2\Delta_2}{\sqrt{(E_{AC} - 2\Delta_2)^2 + 2\Delta_3^2}}, \quad c_2 = \frac{\sqrt{2}\Delta_3}{\sqrt{(E_{AC} - 2\Delta_2)^2 + 2\Delta_3^2}}, \quad (\text{B5})$$

with $c_1^2 + c_2^2 = 1$. The eigenvalue of H_0 λ_i corresponds to the energy of the real band edges. If we focus only on the band structure, a good approximation is to neglect the s - p_z mixing, which yields a correction to the band edges of less than 10^{-3} meV compared to the real ones. By taking the conduction

band as the energy origin, namely $\lambda_e = 0$, we have

$$\lambda_A \simeq E_A = -E_g, \quad (\text{B6})$$

$$\lambda_B \simeq E_B = -E_g - E_{AB}, \quad (\text{B7})$$

$$\lambda_C \simeq E_C = -E_g - E_{AC}, \quad (\text{B8})$$

which directly maps to the band description in Fig. 1(a) (solid curves). Note that, to obtain the basis functions shown in Table IV, we need to perform an exact numerical calculation of the band edge energies.

The 8×8 matrix Hamiltonian in the diagonal basis is given by

$$H_{8 \times 8} = \frac{p^2}{2m_0} + \begin{pmatrix} \lambda_e & i\alpha_{\text{bulk}}k_- & -A_1 \frac{P_2}{\sqrt{2}}k_+ & 0 & if_{\lambda_e \lambda_B}k_- & \frac{1}{2}(g_{\lambda_e \lambda_B}k_z + k_z g_{\lambda_e \lambda_B}) & if_{\lambda_e \lambda_C}k_- & \frac{1}{2}(g_{\lambda_e \lambda_C}k_z + k_z g_{\lambda_e \lambda_C}) \\ -i\alpha_{\text{bulk}}k_+ & \lambda_e & 0 & A_1 \frac{P_2}{\sqrt{2}}k_- & \frac{1}{2}(g_{\lambda_e \lambda_B}k_z + k_z g_{\lambda_e \lambda_B}) & -if_{\lambda_e \lambda_B}k_+ & \frac{1}{2}(g_{\lambda_e \lambda_C}k_z + k_z g_{\lambda_e \lambda_C}) & -if_{\lambda_e \lambda_C}k_+ \\ -if_{\lambda_e \lambda_B}k_+ & -\frac{1}{2}(g_{\lambda_e \lambda_B}k_z + k_z g_{\lambda_e \lambda_B}) & \lambda_A & 0 & 0 & 0 & 0 & 0 \\ -\frac{1}{2}(g_{\lambda_e \lambda_B}k_z + k_z g_{\lambda_e \lambda_B}) & if_{\lambda_e \lambda_B}k_- & 0 & \lambda_A & 0 & 0 & 0 & 0 \\ -if_{\lambda_e \lambda_C}k_+ & -\frac{1}{2}(g_{\lambda_e \lambda_C}k_z + k_z g_{\lambda_e \lambda_C}) & 0 & 0 & \lambda_B & 0 & 0 & 0 \\ -\frac{1}{2}(g_{\lambda_e \lambda_C}k_z + k_z g_{\lambda_e \lambda_C}) & if_{\lambda_e \lambda_C}k_- & 0 & 0 & 0 & \lambda_B & 0 & 0 \\ -A_1 \frac{P_2}{\sqrt{2}}k_- & 0 & 0 & 0 & 0 & 0 & \lambda_C & 0 \\ 0 & A_1 \frac{P_2}{\sqrt{2}}k_+ & 0 & 0 & 0 & 0 & 0 & \lambda_C \end{pmatrix}. \quad (\text{B9})$$

The coefficient α_{bulk} is the bulk Rashba parameter,

$$\alpha_{\text{bulk}} = 2A_1^2 P_2 \Delta_{sz} \left(\frac{c_1^2}{E_g + E_{AB} + \lambda_e} + \frac{c_2^2}{E_g + E_{AC} + \lambda_e} \right). \quad (\text{B10})$$

If we properly expand the expression above, we can recover

the result in Eq. (14).

The parameters $f_{\lambda_e \lambda_i=B,C}$ and $g_{\lambda_e \lambda_i=B,C}$ in Eq. (B9) are defined as

$$f_{\lambda_e \lambda_i} = A_{\lambda_e} A_{\lambda_i} \left[c_1^2 \left(\frac{1}{E_g + E_{AB} + \lambda_e} + \frac{1}{E_g + E_{AB} + \lambda_i} \right) + c_2^2 \left(\frac{1}{E_g + E_{AC} + \lambda_e} + \frac{1}{E_g + E_{AC} + \lambda_i} \right) \right], \quad (\text{B11})$$

and

$$g_{\lambda_e \lambda_i} = \sqrt{2} A_{\lambda_e} A_{\lambda_i} c_1 c_2 P_1 \Delta_{sz} \left[\left(\frac{1}{E_g + E_{AB} + \lambda_i} - \frac{1}{E_g + E_{AB} + \lambda_e} \right) - \left(\frac{1}{E_g + E_{AC} + \lambda_i} - \frac{1}{E_g + E_{AC} + \lambda_e} \right) \right]. \quad (\text{B12})$$

2. Strained case

In the presence of strain, u_{i0} is obtained by diagonalizing the strained CC-basis Kane Hamiltonian (see Sec. II B 3). Therefore, the diagonal basis set is strain dependent.

To construct the Kane model using the diagonal basis in the presence of strain, we need to know how the band edges change compared to the unstrained case. One can obtain these by numerically diagonalizing the Hamiltonian. Here, however, we show the analytical expressions within the approximation of neglecting the s - p_z mixing, since its energy correction is negligibly small. The band edge shift due to strain at the Γ point is schematically shown in Fig. 1(a) (dashed curves), where we have, $E_e^s = E_e + a_{c_1} \varepsilon_{zz} + a_{c_2} (\varepsilon_{xx} + \varepsilon_{yy})$, $E_A^s = E_A + S_1 + S_2$, $E_B^s = E_A^s - E_{AB}^s$, and $E_C^s = E_A^s - E_{AC}^s$. The energy differences between the valence bands in the presence of strain E_{AB}^s , E_{AC}^s , and E_{BC}^s read

$$E_{AB}^s = \frac{1}{2} (\Delta_{\text{cr}} + 3\Delta_2 + S_2) - \frac{1}{2} \sqrt{(\Delta_{\text{cr}} - \Delta_2 + S_2)^2 + 8\Delta_3^2}, \quad (\text{B13})$$

$$E_{AC}^s = \frac{1}{2} (\Delta_{\text{cr}} + 3\Delta_2 + S_2) + \frac{1}{2} \sqrt{(\Delta_{\text{cr}} - \Delta_2 + S_2)^2 + 8\Delta_3^2}, \quad (\text{B14})$$

$$E_{BC}^s = E_{AC}^s - E_{AB}^s = \sqrt{(\Delta_{\text{cr}} - \Delta_2 + S_2)^2 + 8\Delta_3^2}. \quad (\text{B15})$$

We can directly compare the expressions above with the unstrained case [Eqs. (B1)–(B3)] and see the corrections due to strain.

The Kane Hamiltonian in the presence of strain is again similar to that of the unstrained case, with the band parameters in Eq. (B9) being replaced by the strained parameters given above.

Table V. Relation between the bulk band edges E_i^{CC} and E_i [Fig. 1(a)], and quantum well offsets δ_i^{CC} and δ_i [Fig. 1(b)], appearing in the diagonal part of the Kane Hamiltonian. The notation refers to the unstrained case; the strained case can be straightforwardly obtained. The superscripts “w” and “b” stand for well and barrier, respectively. For the expression of energy separations E_{AB} (E_{AB}) and E_{AC} (E_{AC}), see Eqs. 9, B1–B3, and B6–B8.

$E_e^{CC} = E_e$	$E_A^{CC} = E_A$	$E_g^{CC} = E_g$
$E_B^{CC} = E_B + E_{AB} - E_{AB}$	$E_C^{CC} = E_C + E_{AC} - E_{AC}$	
$\delta_e^{CC} = \delta_e$	$\delta_B^{CC} = \delta_B + (E_{AB}^w - E_{AB}^w) - (E_{AB}^b - E_{AB}^b)$	
$\delta_A^{CC} = \delta_A$	$\delta_C^{CC} = \delta_C + (E_{AC}^w - E_{AC}^w) - (E_{AC}^b - E_{AC}^b)$	

Appendix C: Folding down approach

For an arbitrary $n \times n$ matrix Hamiltonian, one can always write the corresponding Schrödinger equation in the compact form

$$\begin{pmatrix} H_P & H_{PQ} \\ H_{PQ}^\dagger & H_Q \end{pmatrix} \begin{pmatrix} \Phi_P \\ \Phi_Q \end{pmatrix} = E \begin{pmatrix} \Phi_P \\ \Phi_Q \end{pmatrix}, \quad (\text{C1})$$

where H_P and H_Q are two subsets of the original matrix, H_{PQ} describes the coupling between these subspaces, and Φ_P and Φ_Q are the corresponding eigenspinors. Here, as shown below, we are interested in the subspace P .

We can use the so-called folding down approach to rewrite Eq. (C1) as

$$\mathcal{H}_P(E) \Phi_P = E \Phi_P, \quad (\text{C2})$$

with

$$\mathcal{H}_P(E) = \left[H_P + H_{PQ} (E - H_Q)^{-1} H_{PQ}^\dagger \right]. \quad (\text{C3})$$

Note that $\mathcal{H}_P(E)$ is energy-dependent, which makes Eq. (C2) not a *real* Schrödinger-type equation.

To ensure norm conservation, we build a new spinor Φ'_p ,

$$\Phi'_p = \Omega \Phi_P, \quad \Omega = \sqrt{1 + H_{PQ} \frac{1}{(E - H_Q)^2} H_{PQ}^\dagger}. \quad (\text{C4})$$

By inserting Φ'_p into Eq. (C2) and multiplying the resulting equation from the left by Ω^{-1} , we arrive at

$$\Omega^{-1} \mathcal{H}_P(E) \Omega^{-1} \Phi'_p = E \Omega^{-2} \Phi'_p. \quad (\text{C5})$$

From Eq. (C5) we obtain

$$\mathcal{H}'_p(E) \Phi'_p = E \Phi'_p, \quad (\text{C6})$$

with

$$\mathcal{H}'_p(E) = [\Omega^{-1} \mathcal{H}_P(E) \Omega^{-1} + E(I - \Omega^{-2})], \quad (\text{C7})$$

where I is the identity matrix, which has the same dimension of the subspace P . From Eq. (C6), it is possible to arrive at a real Schrödinger-type equation, i.e., $\mathcal{H}'_p(E) \rightarrow \mathcal{H}'_p$ energy independent, by performing a power expansion of $(E - H_Q)^{-1}$ up to the second order in the energy E .

By using the procedure described above, we obtain exactly the same result as in Eqs. (24)–(30).

Appendix D: $k \cdot p$ interaction within the valence band subspace

The 6×6 Hamiltonian (CC basis) for the p valence band including the $k \cdot p$ interaction within its subspace is given by

$$H_V = \frac{p^2}{2m_0} + \begin{pmatrix} -E_g + V_A(z) & 0 & 0 & 0 & \frac{iQ}{\sqrt{2}}k_- & 0 \\ 0 & -E_g + V_A(z) & 0 & 0 & 0 & -\frac{iQ}{\sqrt{2}}k_+ \\ 0 & 0 & -E_g - E_{AB} + V_B(z) & 0 & -\frac{iQ}{\sqrt{2}}k_+ & \sqrt{2}\Delta_3 \\ 0 & 0 & 0 & -E_g - E_{AB} + V_B(z) & \sqrt{2}\Delta_3 & \frac{iQ}{\sqrt{2}}k_+ \\ -\frac{iQ}{\sqrt{2}}k_+ & 0 & \frac{iQ}{\sqrt{2}}k_- & \sqrt{2}\Delta_3 & -E_g - E_{AC} + V_C(z) & 0 \\ 0 & \frac{iQ}{\sqrt{2}}k_- & \sqrt{2}\Delta_3 & -\frac{iQ}{\sqrt{2}}k_+ & 0 & -E_g - E_{AC} + V_C(z) \end{pmatrix}, \quad (D1)$$

with Q being defined as $Q = -(i\hbar/m_0)\langle Z' | p_x | X \rangle = -(i\hbar/m_0)\langle Z' | p_y | Y \rangle$. The additional Rashba terms arising from the $k \cdot p$ interaction inside the valence band subspace read

$$H_R^Q = \eta_Q(z)(\sigma_x k_y - \sigma_y k_x), \quad (D2)$$

with

$$\eta_Q(z) = \frac{P_1 Q \Delta_{sz}}{(E_g + 2\Delta_2)^2 (E_g + \Delta_1 + \Delta_2)} \frac{dV_B(z)}{dz} + \frac{P_1 Q \Delta_{sz}}{(E_g + 2\Delta_2)(E_g + \Delta_1 + \Delta_2)^2} \frac{dV_C(z)}{dz} + \frac{4\Delta_{sz}^2 \Delta_3 Q}{(E_g + 2\Delta_2)^2 (E_g + \Delta_1 + \Delta_2)}, \quad (D3)$$

where one can see that these terms also depend on the s - p_z mixing, i.e., Δ_{sz} . The first two terms in the equation above describe the usual Rashba coupling. By assuming that the Kane parameters P_2 and Q are comparable, we find that the strength of these terms is around one tenth of that of η_H and η_w discussed in the main text [see Eqs. (33) and (34)]. The last term contributes to the bulk Rashba term and has a negligible value when compared to (14).

In addition, we shall point out that here we also obtain the Dresselhaus term,

$$H_D = \beta_D (bk_z^2 - k_{\parallel}^2)(\sigma_x k_y - \sigma_y k_x), \quad (D4)$$

with the coefficients $\beta_D \equiv \beta_{D1} + \beta_{D2}$ and b defined as

$$\beta_{D1} = -\frac{P_2^3 \Delta_{sz}}{E_g + E_{AB}} \left(\frac{1}{E_g^2} + \frac{1}{(E_g + E_{AB})^2} + \frac{1}{(E_g + E_{AC})^2} \right), \quad (D5)$$

$$\beta_{D2} = \frac{P_2 Q (Q \Delta_{sz} + P_2 \Delta_3)}{(E_g + E_{AB})(E_g + E_{AC})} \left(\frac{1}{E_g} + \frac{1}{E_g + E_{AB}} \right), \quad (D6)$$

and

$$b = \frac{2P_1^2 \Delta_3}{\beta_D (E_g + E_{AB})(E_g + E_{AC})} \left(\frac{Q \Delta_3 - P_2 \Delta_{sz}}{E_g + E_{AC}} - \frac{P_2 \Delta_{sz}}{E_g + E_{AB}} \right). \quad (D7)$$

The constants β_{D1} and β_{D2} describe the bulk Dresselhaus coefficients. The former arises entirely from the s - p_z mixing and does not depend on Q and the latter is determined by Q . It is worth mentioning that the s - p_z mixing also partially contributes to β_{D2} [see Eq. (D6)]. The parameter b implies the nonequivalence between the c axis orientated z direction and the x - y plane.

We must emphasize that the Dresselhaus term here was obtained within the eight-band model (s -conduction and p -valence bands). This is in contrast to the zincblende structure, in which the Dresselhaus term is associated with the coupling between the p -valence and p -conduction bands. On the other hand, from Eqs. (D5)–(D7) we evaluate $\beta_D \sim 0.08 \text{ meV} \cdot \text{\AA}^3$ and $b \sim 0.01$, whose values are much smaller than the semi-empirical values $\beta_D \sim 0.32 \text{ meV} \cdot \text{\AA}^3$ and $b \sim 4.0$ [24]. Further studies to obtain the full expression of the Dresselhaus term accounting for the other remote bands are needed. As mentioned in the main text, in this work we add the Dresselhaus coupling by hand into our self-consistent simulation and treat the coefficients β_D and b in Eq. (D4) as semi-empirical parameters.

Appendix E: Total Hartree potential

The total Hartree potential, given in Eq. (23) of the main text, has several contributions (these arise from different charge densities): V_{elect} , V_{int} , V_d , and V_g . Here we explicitly show how to determine each one of these terms from the Poisson equation.

1. Pure Hartree potential: V_{elect}

The pure Hartree potential V_{elect} is obtained by solving

$$\frac{d^2}{dz^2} V_{\text{elect}}(z) = \frac{e}{\epsilon_0 \epsilon_r} \rho_e(z), \quad (\text{E1})$$

together with the Dirichlet boundary conditions $V_{\text{elect}}(\pm L) = 0$, where $\pm L$ are the end points of our system (see Fig. E.1) and $e > 0$ is the elementary charge. The parameter $\rho_e(z)$ corresponds to the electronic charge density and reads

$$\rho_e(z) = -\frac{2e}{A} \sum_{\nu, k_{\parallel}} |e^{i\mathbf{k}_{\parallel} \cdot \mathbf{r}} \psi_{\nu}(z)|^2 f(\mathcal{E}_{k_{\parallel\nu}}), \quad (\text{E2})$$

with A the area of the electron gas in the xy -plane (normalizing constant) and $f(\mathcal{E}_{k_{\parallel\nu}})$ the Fermi-Dirac distribution. More explicitly,

$$\rho_e(z) = -\frac{em^*}{\pi \hbar^2} k_B T \sum_{\nu} |\psi_{\nu}(z)|^2 \ln \left[1 + e^{(\mu - \mathcal{E}_{\nu})/k_B T} \right], \quad (\text{E3})$$

in which k_B is the Boltzmann constant, T is the temperature, and μ is the chemical potential.

We shall point that $\rho_e(z)$ in Eq. (E1) depends on the wave functions $\psi_{\nu}(z)$ [see Eq. (E3)], which were obtained by solving the Schrödinger equation for the quantum well (25). This equation depends on the total potential $V_e(z)$, which in turn has $V_{\text{elect}}(z)$ as one of its contributions. Hence, to determine $\psi_{\nu}(z)$ and $\rho_e(z)$, we self-consistently solve Schrödinger and Poisson's equations for the total charge density (see next sections for the other charge density contributions).

2. Internal potential: V_{int}

The internal potential V_{int} due to the built-in electric field is written as

$$V_{\text{int}}(z) = e \int_{-L}^z E_{\text{int}}(z') dz', \quad (\text{E4})$$

where $E_{\text{int}}(z')$ can be either E_w or E_b given in Eqs. (19) (periodic boundary conditions) or (20) (neutral surface charges). The solutions in terms of the fields read

$$V_{\text{int}}(z) = \begin{cases} eE_b(z+L), & -L \leq z \leq -L_w/2 \\ eE_b\left(L - \frac{L_w}{2}\right) + eE_w\left(z + \frac{L_w}{2}\right), & -L_w/2 \leq z \leq L_w/2 \\ eE_b(z+L-L_w) + eE_w L_w. & L_w/2 \leq z \leq L \end{cases} \quad (\text{E5})$$

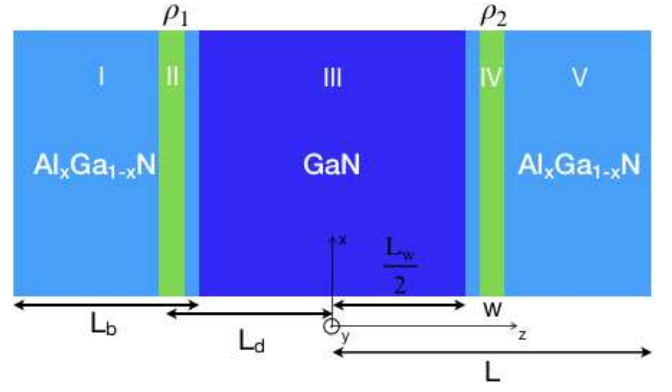


Figure E.1. Schematic of a GaN/Al_xGa_{1-x}N quantum well grown along the $z \parallel [0001]$ direction. The well region and the two symmetric barriers have widths $L_w = 10$ nm and $L_b = 7$ nm, respectively. The gray regions correspond to two doping layers of densities ρ_1 and ρ_2 and width w , symmetrically located at $L_d = 6$ nm from the center of the well. The total width of the system is $2L$.

3. Doping + external gate potentials: $V_d + V_g$

These two contributions can be obtained by solving the Poisson equation + boundary conditions in each region (I–V) of our system (Fig. E.1) [20].

For the doping potential V_d we have

$$\frac{d^2}{dz^2} V_d(z) = \frac{e^2}{\epsilon_0 \epsilon_r} \begin{cases} 0, & -L \leq z \leq -L_d & \text{(I)} \\ \rho_1, & -L_d \leq z \leq -L_d + w & \text{(II)} \\ 0, & -L_d + w \leq z \leq L_d - w & \text{(III)} \\ \rho_2, & L_d - w \leq z \leq L_d & \text{(IV)} \\ 0, & L_d \leq z \leq L & \text{(V)} \end{cases} \quad (\text{E6})$$

where $\rho_{1,2}$ are the doping densities. The solutions to the equations above are given by

$$V_d(z) = \begin{cases} a_1 z + a_2, & \text{(I)} \\ \frac{e^2 \rho_1}{2\epsilon_0 \epsilon_r} z + a_3 z + a_4, & \text{(II)} \\ a_5 z + a_6, & \text{(III)} \\ \frac{e^2 \rho_2}{2\epsilon_0 \epsilon_r} z + a_7 z + a_8, & \text{(IV)} \\ a_9 z + a_{10}. & \text{(V)} \end{cases} \quad (\text{E7})$$

The coefficients a_i , $i = 1, \dots, 10$, are obtained by imposing the continuity of V_d and its derivative. In addition, we consider the Dirichlet boundary conditions $V_d(\pm L) = 0$. The explicit expressions for these constants can be found in Appendix B of Ref. [20].

For the external gate potential V_g , we solve

$$\frac{d^2}{dz^2} V_g(z) = 0, \quad -L \leq z \leq L \quad (\text{E8})$$

with the Dirichlet boundary conditions $V_g(-L) = V_1$ and $V_g(L) = V_2$, where $V_{1,2}$ are the external gates at the end points $\pm L$. We then obtain

$$V_g(z) = -\frac{(V_1 - V_2)}{2L} z + \frac{(V_1 + V_2)}{2}. \quad (\text{E9})$$

- [1] D. Awschalom, D. Loss, and N. Samarth, *Semiconductor Spintronics and Quantum Computation* (Springer, New York, 2002).
- [2] I. Žutić, J. Fabian, S. D. Sarma, *Rev. Mod. Phys.* **76**, 323 (2004).
- [3] C. L. Kane and E. J. Mele, *Phys. Rev. Lett.* **95**, 226801 (2005).
- [4] B. A. Bernevig, T. L. Hughes, and S. C. Zhang, *Science* **314**, 1757 (2006).
- [5] Jason Alicea, *Phys. Rev. B* **81**, 125318 (2010).
- [6] R. M. Lutchyn, J. D. Sau, and S. D. Sarma, *Phys. Rev. Lett.* **105**, 077001 (2010).
- [7] Y. Oreg, G. Refael, and F. Oppen, *Phys. Rev. Lett.* **105**, 177002 (2010).
- [8] H. M. Weng, C. Fang, Z. Fang, B. A. Bernevig, and X. Dai, *Phys. Rev. X* **5**, 011029 (2015).
- [9] F. Dettwiler, J. Y. Fu, S. Mack, P. J. Weigele, J. Carlos Egues, D. D. Awschalom, and D. M. Zumbühl, *Phys. Rev. X* **7**, 031010 (2017).
- [10] J. Schliemann, J. Carlos Egues, and D. Loss, *Phys. Rev. Lett.* **90**, 146801 (2003).
- [11] B. A. Bernevig, J. Orenstein, and S. C. Zhang, *Phys. Rev. Lett.* **97**, 236601 (2006).
- [12] J. D. Koralek, C. P. Weber, J. Orenstein, B. A. Bernevig, S. C. Zhang, S. Mack, and D. D. Awschalom, *Nature* **458**, 610 (2009).
- [13] M. P. Walser, C. Reichl, W. Wegscheider, and G. Salis, *Nature Physics* **8**, 757 (2012).
- [14] Jiyong Fu, Poliana H. Penteado, Marco O. Hachiya, Daniel Loss, and J. Carlos Egues, *Phys. Rev. Lett.* **117**, 226401 (2016).
- [15] Jiyong Fu and J. Carlos Egues, *Phys. Rev. B* **91**, 075408 (2015).
- [16] R. Winkler, *Spin-Orbit Coupling Effects in Two-Dimensional Electron and Hole Systems* (Springer, Berlin, 2003)
- [17] Y. A. Bychkov and E. I. Rashba, *Pis'ma Zh. Eksp. Teor. Fiz.* **39**, 66 (1984) [*Sov. Phys. JETP Lett.* **39**, 78 (1984)].
- [18] G. Dresselhaus, *Phys. Rev.* **100**, 580 (1955).
- [19] E. S. Bernardes, J. Schliemann, M. Lee, J. Carlos Egues, and D. Loss, *Phys. Rev. Lett.* **90**, 076603 (2007).
- [20] R. S. Calsaverini, E. Bernardes, J. Carlos Egues, and D. Loss, *Phys. Rev. B* **78**, 155313 (2008).
- [21] E. I. Rashba and V. I. Sheka, *Fiz. Tverd. Tela: Collected Papers* **2**, 162 (1959).
- [22] G. Bihlmayer, O. Rader, and R. Winkler, *New J. Phys.* **17**, 050202 (2015).
- [23] W. T. Wang, C. L. Wu, S. F. Tsay, M. H. Gau, I. Lo, H. F. Kao, D. J. Jang, J. C. Chiang, M. E. Lee, Y. C. Chang, C. N. Chen, and H. C. Hsueh, *Appl. Phys. Lett.* **91**, 082110 (2007).
- [24] J. Y. Fu and M. W. Wu, *J. Appl. Phys.* **104**, 093712 (2008).
- [25] W. Weber, S. D. Ganichev, S. N. Danilov, D. Weiss, W. Prettl, Z. D. Kvon, V. V. Belkov, L. E. Golub, H. I. Cho, and J. H. Lee, *Appl. Phys. Lett.* **87**, 262106 (2005).
- [26] S. Schmult, M. J. Manfra, A. Punnoose, A. M. Sergent, K. W. Baldwin, and R. J. Molnar, *Phys. Rev. B* **74**, 033302 (2006).
- [27] N. Thillosen, Th. Schäpers, N. Kaluza, H. Hardtdegen, and V. A. Guzenko, *Appl. Phys. Lett.* **88**, 022111 (2006).
- [28] C. Kurdak, N. Biyikli, Ü. Özgür, H. Morkoç, and V. I. Litvinov, *Phys. Rev. B* **74**, 113308 (2006).
- [29] I. Lo, M. H. Gau, J. K. Tsay, Y. L. Chen, Z. J. Chang, W. T. Wang, J. C. Chiang, T. Aggerstam and S. Lourdudoss, *Phys. Rev. B* **75**, 245307 (2007).
- [30] A. E. Belyaev, V. G. Raicheva, A. M. Kurakin, N. Klein, and S. A. Vitusevich, *Phys. Rev. B* **77**, 035311 (2008).
- [31] E. B. Olshanetsky, Z. D. Kvon, S. Sassine, J. C. Portal, H. I. Cho, and J. H. Lee, *Appl. Phys. Lett.* **92**, 242112 (2008).
- [32] H. Cheng a, N. Biyikli, Ü. Özgür, C. Kurdak, H. Morkoç, V. I. Litvinov, *Physica E* **40**, 1586 (2008).
- [33] S. B. Lisesivdin, N. Balkan, O. Makarovskiy, A. Patane, A. Yildiz, M. D. Caliskan, M. Kasap, S. Ozelcik, and E. Ozbay, *J. Appl. Phys.* **105**, 093701 (2009).
- [34] W. Stefanowicz, R. Adhikari, T. Andrearczyk, B. Faina, M. Sawicki, J. A. Majewski, T. Dietl, and A. Bonanni, *Phys. Rev. B* **89**, 205201 (2014).
- [35] L. C. Lew Yan Voon, M. Willatzen, M. Cardona, and N. E. Christensen, *Phys. Rev. B* **53**, 10703 (1996).
- [36] V. I. Litvinov, *Phys. Rev. B* **68**, 155314 (2003).
- [37] N. Thillosen, S. Cabañas, N. Kaluza, V. A. Guzenko, H. Hardtdegen, and Th. Schäpers, *Phys. Rev. B* **73**, 241311(R) (2006).
- [38] Th. Schäpers, N. Thillosen, S. Cabañas, N. Kaluza, V. A. Guzenko, and H. Hardtdegen, *Phys. Rev. B* **73**, 241311(R) (2006).
- [39] E. I. Rashba, *Sov. Phys.-Solid State* **1**, 368 (1959).
- [40] C. Yin, B. Shen, Q. Zhang, F. J. Xu, N. Tang, L. B. Cen, X. Q. Wang, Y. H. Chen, and J. L. Yu, *Appl. Phys. Lett.* **97**, 181904 (2010).
- [41] P. E. Faria Junior, T. Campos, C. M. O. Bastos, M. Gmitra, J. Fabian, and G. M. Sipahi, *Phys. Rev. B* **93**, 235204 (2016).
- [42] J.A. Majewski, *Acta Physica Polonica A* **108**, 777 (2005).
- [43] V. I. Litvinov, *Appl. Phys. Lett.* **89**, 222108 (2006).
- [44] S. L. Chuang and C. S. Chang, *Phys. Rev. B* **54**, 2491 (1996).
- [45] P. Löwdin, *J. Phys. Chem.* **19**, 1396 (1951).
- [46] M. Li, R. Zhang, Z. Zhang, B. Liu, D. Y. Fu, C. Z. Zhao, Z. L. Xie, X. Q. Xiu, and Y. D. Zheng, *Phys. Status Solidi B* **248**, 187 (2011).
- [47] M. Li, Y. H. Lv, B. H. Yang, Z. Y. Zhao, G. Sun, D. D. Miao, C. Z. Zhao, *Solid State Commun.* **151**, 1958 (2011).
- [48] M. Cardona, N. E. Christensen, and G. Fasol, *Phys. Rev. B* **38**, 1806 (1988).
- [49] The bulk contribution to the Rashba coupling in our wells, essentially refers to *weighted* (i.e., averaged) bulk contributions from both the well and barrier layers.
- [50] E. Q. Kane, *J. Phys. Chem. Solids.* **1**, 249 (1957).
- [51] L. C. Lew Yan Voon and M. Willatzen, *The k-p method – Electronic properties of semiconductors* (Springer, New York, 2009).
- [52] G. L. Bir and G. E. Pikus, *Symmetry and Strain-Induced Effects in Semiconductors* (John Wiley and Sons, New York, 1974).
- [53] T. B. Bahder, *Phys. Rev. B* **41**, 11992 (1990).
- [54] This procedure is equivalent to including only first order terms in the Löwdin expansion [16].
- [55] G. B. Ren, Y. M. Liu, and P. Bloodb, *Appl. Phys. Lett.* **74**, 1117 (1999).
- [56] M. J. Reed, N. A. Masry, C. A. Parker, J. C. Roberts, and S. M. Bedair, *Appl. Phys. Lett.* **77**, 4121 (2000).
- [57] J. S. Im, H. Kollmer, J. Off, A. Sohmer, F. Scholz, and A. Hangleiter, *Phys. Rev.* **57**, R9435 (1997).
- [58] I. Vurgaftman, J. R. Meyer, L. R. Ram-Mohan, *J. Appl. Phys.* **89**, 5815 (2001).
- [59] W. Shan, R. J. Hauenstein, A. J. Fischer, J. J. Song, W. G. Perry, M. D. Bremser, R. F. Davis, and B. Goldenberg, *Phys. Rev. B* **54**, 13460 (1996).
- [60] G. Bastard, *Wave Mechanics Applied to Semiconductor Heterostructures* (Halsted, Les Ulis, France, 1988).
- [61] M. G. Burt, *Semicond. Sci. Technol.* **3**, 739 (1988).
- [62] O. Ambacher, J. Majewski, C. Miskys, A. Link, M. Hermann, M. Eickhoff, M. Stutzmann, F. Bernardini, V. Fiorentini, V.

- Tilak, B. Schaff, and L. F. Eastman, *J. Phys.: Condens. Matter* **14**, 3399 (2002).
- [63] J. Majewski, G. Zandler, and P. Vogl, *J. Phys.: Condens. Matter* **14**, 3511 (2002).
- [64] N. Grandjean, B. Damilano, S. Dalmaso, M. Leroux, M. Laigt, and J. Massies, *J. Appl. Phys.* **86**, 3714 (1999).
- [65] G. Martin, A. Botchkarev, A. Rockett, and H. Morko, *Appl. Phys. Lett.* **68**, 2541 (1996).
- [66] T. H. Yu and K. F. Brennan, *J. Appl. Phys.* **89**, 3827 (2001).
- [67] Since $V_e = V_H + \delta_e h_w(z)$ and $V_B = V_H - \delta_B h_w(z)$ (see Sec. II C), we have $V_e - V_B = (\delta_e + \delta_B) h_w(z)$. Therefore, for $|z| < L_w/2$ [$h_w(z) = 0$], $\eta(z) = \alpha_{\text{bulk}}(\text{well}) = 2P_2\Delta_{sz}/(E_g + 2\Delta_2)$; for $|z| > L_w/2$ [$h_w(z) = 1$], $\eta(z) = [2P_2\Delta_{sz}/(E_g + 2\Delta_2)][1 - (\delta_e + \delta_B)/(E_g + 2\Delta_2)]$, which is exactly the Taylor expansion of $\alpha_{\text{bulk}}(\text{well}) = 2P_2\Delta_{sz}/(E_g + 2\Delta_2 + \delta_e + \delta_B)$, up to the second order in $(\delta_e + \delta_B)/(E_g + 2\Delta_2)$.
- [68] D. J. Dugdale, S. Brand, and R. A. Abram, *Phys. Rev. B* **61**, 12933 (2000).
- [69] A. Dargys, *Phys. Rev. B* **72**, 045220 (2005).
- [70] J.J. Sakurai, *Advanced Quantum Mechanics* (Addison-Wesley, Reading, MA, 1967).
- [71] M. W. Wu, J. H. Jiang, and M. Q. Weng, *Phys. Rep.* **493**, 61 (2010).
- [72] S. D. Ganichev and L. E. Golub, *Phys. Status Solidi B* **251**, 1801 (2014).
- [73] S. H. Park and S. L. Chuang, *Appl. Phys. Lett.* **76**, 1981 (2000).
- [74] E. P. Pokatilov, D. L. Nika, V. M. Fomin, and J. T. Devreese, *Phys. Rev. B* **77**, 125328 (2008).
- [75] A. Polian, M. Grimsditch, and I. Grzegory, *J. Appl. Phys.* **79**, 3343 (1996).
- [76] The s - p_z mixing modifies the S (conduction subband) and the Z (valence band) wave functions, which can be written as $|S\rangle \rightarrow |S'\rangle = q_s|S\rangle + q_z|Z\rangle$ and $|Z\rangle \rightarrow |Z'\rangle = q_s|Z\rangle - q_z|S\rangle$, with $q_s^2 + q_z^2 = 1$ [35]. Based on the new wave functions and the definition of Δ_{sz} by Eq. (8), one can straightforwardly obtain $\Delta_{sz} = q_z\Delta_3$. Here we consider $q_z = 0.1$.
- [77] J. S. Im, H. Kollmer, J. Off, A. Sohmer, F. Scholz, and A. Hangleiter, *Phys. Rev. B* **57**, R9435 (1998).
- [78] O. Ambacher, J. Smart, J. R. Shealy, N. G. Weimann, K. Chu, M. Murphy, W. J. Schaff, L. F. Eastman, R. Dimitrov, L. Wittmer, M. Stutzmann, W. Rieger, and J. Hilsenbeck, *J. Appl. Phys.* **85**, 3222 (1999).
- [79] Q. M. Yan, P. Rinke, M. Winkelkemper, A. Qteish, D. Bimberg, M. Scheffler, and C. G. Van de Walle, *Semicond. Sci. Technol.* **26**, 014307 (2011).
- [80] S. H. Park and S. L. Chuang, *Appl. Phys. Lett.* **72**, 3103 (1998).
- [81] A. S. Barker, Jr. and M. Ilegems, *Phys. Rev. B* **7**, 743 (1973).
- [82] S. H. Park and S. L. Chuang, *J. Appl. Phys.* **87**, 353 (2000).
- [83] H. M. Ng, R. Harel, S.N.G. Chu, and A.Y. Cho, *J. Elec. Mater.* **30**, 134 (2001).
- [84] M. I. Aroyo, J. M. Perez-Mato, D. Orobengoa, E. Tasci, G. de la Flor, and A. Kirov, *Bulg. Chem. Commun.* **43**(2) 183-197 (2011).
- [85] M. I. Aroyo, J. M. Perez-Mato, C. Capillas, E. Kroumova, S. Ivantchev, G. Madariaga, A. Kirov, and H. Wondratschek, *Z. Krist.* **221**, 1, 15-27 (2006).
- [86] M. I. Aroyo, A. Kirov, C. Capillas, J. M. Perez-Mato, and H. Wondratschek, *Acta Cryst. A* **62**, 115-128 (2006).
- [87] Daniel Varjas, Tomas ˆ. Rosdahl, and Anton R. Akhmerov, *New J. Phys.* **20**, 093026 (2018).
- [88] R. C. Casella, *Phys. Rev.* **114**, 1514 (1959).